

# Concurrent Fermionic Simulation Gate

Zhongyi Jiang and Mohammad H. Ansari

*Peter Grünberg Institute (PGI-2), Forschungszentrum Jülich, Jülich 52428, Germany and  
Institute for Quantum Information, RWTH Aachen University, D-52056 Aachen, Germany*

(Dated: December 2, 2024)

Introducing flexible native entanglement gates can significantly reduce circuit complexity. We propose a novel gate integrating iswap and cphase operations within a single gate cycle. We theoretically show one possible realization of this gate for superconducting qubits using bichromatic parametric drives at distinct frequencies. We show how various parameters, such as drive amplitudes and frequencies, can control entanglement parameters. This approach enhances gate versatility, opening pathways for more efficient quantum computing.

## CONTENTS

I. Introduction	1
II. The Concept	2
III. Concurrent fermionic simulation gate	3
A. Setup: bichromatic parametric driving (BPD)	3
B. Weak BPD	4
C. Strong BPD	5
1. Monochromatic parametric driving case	6
IV. Crosstalk in BPD	8
V. Optimization and Results	8
VI. Concurrency in the cfSim gate	10
VII. ZZ-free iswap in the cfSim	11
VIII. Summary	12
Acknowledgments	13
A. Bogoliubov Approach	14
B. Analytical coupling strength by exact diagonalization	14
C. Details of crosstalk	16
D. Minimizing Leakage	16
E. Pulse Shaping	16
References	18

## I. INTRODUCTION

Quantum computing has made remarkable progress, achieving milestones such as quantum error correction, which enables practical computation despite challenges like decoherence [1]. Modern quantum processors now support around 100 qubits, and quantum supremacy

demonstrations have shown limited speedups [2, 3]. As highlighted recently in Ref. [4], the next goal is achieving quantum utility by efficiently solving practical problems. This requires significant advancements in the challenges for 100-1M physical qubit processors, such as qubit coherence, gate accuracy and compactification [4, 5].

A quantum processor is considered universal if it can simulate any quantum circuit to arbitrary accuracy using a finite set of gates acting on a finite number of qubits. This requires single-qubit Hamiltonians to generate all  $SU(2)$  gates and at least one two-qubit interaction to produce entangling gates [6–9]. Discussions of universality often focus on unitary gates (exponentiated Hamiltonians) rather than physical Hamiltonians.

Recent technological advancements for controlling non-unitary errors, e.g. nonequilibrium quasiparticle tunneling [10–13] and trap state noise [14, 15], as well as unitary errors, e.g. ZZ stray couplings [16–18], have improved gate fidelity, architecture, and manufacturing, have enabled problem-specific algorithms to leverage quantum computing’s power [3, 19–25]. These developments have set the stage for high-fidelity computing with thousands of qubits. Two most applicable two-qubit gates are iswap (swapping  $|01\rangle \leftrightarrow |10\rangle$ ) and cphase (applying a  $\pi$  phase to  $|11\rangle$ ). Often, a small cphase is a byproduct of iswap and vice versa. However, it has been shown recently that one can better control the cphase byproduct of iswap to define a new gate, namely ‘fermionic Simulation (fSim).’ This new gate can be separated into two gates in certain conditions.

The fSim gate is a versatile quantum computing tool, particularly useful for simulating phase transitions in strongly correlated fermionic systems [26–28]. Combining the functionality of two gates reduces resource demands and enhances flexibility for parameter-specific applications.

The fSim gate has been implemented in superconducting qubits using bichromatic modulation of frequency detuning and coupling strengths or hybrid methods with parametric drives [29, 30]. These approaches enable continuous transformations, swapping  $|01\rangle$  and  $|10\rangle$  while introducing a controllable phase for  $|11\rangle$ . The gate’s parameters  $\theta$  and  $\varphi$  allow state swaps and apply a phase factor  $\exp(i\varphi)$ , as represented by:

## II. THE CONCEPT

$$\widehat{\text{fSim}}(\theta, \varphi) = \begin{pmatrix} 1 & 0 & 0 & 0 \\ 0 & \cos(\theta) & -i \sin(\theta) & 0 \\ 0 & -i \sin(\theta) & \cos(\theta) & 0 \\ 0 & 0 & 0 & e^{i\varphi} \end{pmatrix} \quad (1)$$

With full control over  $\theta$  (0 to  $90^\circ$ ) and  $\varphi$  (0 to  $180^\circ$ ), the fSim gate mimics anti-commuting particles. It improves the Quantum Approximate Optimization Algorithm (QAOA) [31] and reduces circuit depth in quantum variational eigensolvers for molecular hydrogen by a factor of 10 compared to controlled-NOT gates [32]. The rotation  $\widehat{\text{fSim}}(\pi/2, \pi)$  simplifies resource use for fermion simulations. Combining native fSim gates with XYZ decomposition and optimized fermion-to-qubit mappings reduces circuit depth by 70% in Fermi-Hubbard model simulations on square lattice quantum processors [33].

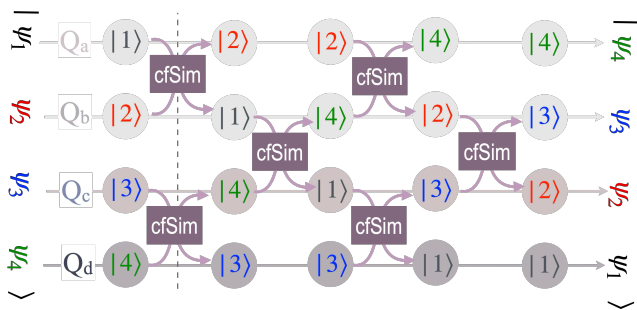


FIG. 1: Representation of 4 fermions  $|\psi_1, \psi_2, \psi_3, \psi_4\rangle$  on a column of 4 qubits  $Q_a, Q_b, Q_c,$  and  $Q_d$ . It takes six two-qubit concurrent fSim (cfSim) gates to transform the initial state into  $|\psi_4, \psi_3, \psi_2, \psi_1\rangle$ .

We propose an efficient theoretical modification to the fSim gate that integrates iswap and phase operations into a single hardware. This enables their simultaneous and controllable application, namely the “concurrent fSim (cfSim).” This approach compresses the gate time of consecutive iswap and cphase operations into one shorter gate with the same output. Our theoretical study demonstrates that this method simultaneously achieves the full range of iswap angles and conditional phases, inherently facilitating a fermion swap in a single operation. For its realization, we employ the example of bichromatic parametric drives at distinct frequencies in a transmon-coupler-transmon setup. The method uses two parametric drives: one resonating with the  $|01\rangle \leftrightarrow |10\rangle$  transition to control the iswap angle, and the other facilitating cphase transitions via  $|11\rangle \leftrightarrow |02\rangle$ ,  $|11\rangle \leftrightarrow |20\rangle$ , or both. Completing an oscillation cycle induces a detuning-dependent phase shift in the  $|11\rangle$  state and reduces leakage at the same time. Moreover, we develop precise analytical strategies to accurately predict transition dynamics and resolve crosstalk between the drives, resolving synchronization issues.

One key application of quantum computing is simulating many-body models. A crucial aspect of state preparation for these systems involves constructing an adjacent fermionic swap network to ensure that many-body states satisfy the anticommutation relations of fermionic states.

Let  $|\psi_1 \cdots \psi_i \cdots\rangle$  represent the state of distinguishable and labeled fermions, where  $\psi_i$  denotes the state of the  $i$ -th fermion. Swapping the states of the first and second fermions in  $|\psi, \phi\rangle$  not only exchanges their states but also introduces a  $\pi$ -rotation phase, i.e.,  $e^{i\pi}|\phi, \psi\rangle$ . More generally, the fermionic swap operator  $\hat{S}_{ij}$  exchanges the states of the  $i$ -th and  $j$ -th fermions with a phase:  $\hat{S}_{ij}|\psi_1 \cdots \psi_i \cdots \psi_j \cdots\rangle = e^{i\pi}|\psi_1 \cdots \psi_j \cdots \psi_i \cdots\rangle$ . Applying  $\hat{S}_{ij}$  twice restores the original state, i.e.,  $\hat{S}_{ij}\hat{S}_{ji} = 1$ . Additionally, as a unitary operator,  $\hat{S}_{ij}$  satisfies  $(\hat{S}_{ij})^\dagger = \hat{S}_{ji}$ .

For tensor networks in classical simulations of fermionic systems [34], the fermionic swap operator can be expressed independently of any specific qubit mapping of fermions. It is defined using the fermionic operators  $\hat{f}_i^\dagger$  (creation) and  $\hat{f}_i$  (annihilation), which act on the vacuum state  $|\text{vac}\rangle_i$  at site  $i$  and satisfy the anticommutation relation  $\{\hat{f}_i, \hat{f}_j^\dagger\} = \delta_{ij}$ . The swap operator satisfies  $\hat{S}_{ij}\hat{f}_i^\dagger\hat{S}_{ij}^\dagger = \hat{f}_j^\dagger$  and  $\hat{S}_{ij}\hat{f}_i\hat{S}_{ij}^\dagger = \hat{f}_j$ . This leads to the explicit form  $\hat{S}_{ij} = \hat{f}_i^\dagger(\hat{f}_j - \hat{f}_i) + \hat{f}_j^\dagger(\hat{f}_i - \hat{f}_j) + 1$ , preserving the anticommutation properties of fermions.

Qubit mapping is a useful transformation representing multi-particle fermionic states using qubits, such as the Jordan-Wigner transformation [35]. This mapping relies on the ordering of operators and qubits.

For instance, fermion states  $|\psi_i\rangle$  can be encoded as qubit states  $|0\rangle_i$  and  $|1\rangle_i$  at site  $i$  with the mapping:

$$\begin{aligned} \text{fermion } |\text{vac}\rangle_i &\leftrightarrow \text{qubit } |0\rangle_i \\ \text{fermion } |\psi_i\rangle &\leftrightarrow \text{qubit } |1\rangle_i \end{aligned} \quad (2)$$

with  $|\psi_i\rangle$  being  $\hat{f}_i^\dagger|\text{vac}\rangle_i$ .

Consider the general fermionic Hamiltonian:  $H = \sum_{ij} A_{ij}\hat{f}_i^\dagger\hat{f}_j + \sum_i B_i\hat{n}_i + \sum_{i \neq j} C_{ij}\hat{n}_i\hat{n}_j$ , with  $\hat{n}_i = \hat{f}_i^\dagger\hat{f}_i$  as the number operator. This Hamiltonian appears in models like the Hubbard model and quantum chemistry, with non-local hopping terms  $A_{ij}$  and four-body interaction terms  $C_{ij}$ . Importantly,  $H$  remains unchanged under  $\hat{S}_{ij}$ , making  $\hat{S}_{ij}$  a symmetry operator. Time evolution under  $H$  can thus incorporate the fermionic swap.

The fermionic swap exchanges  $\psi_i$  and  $\psi_j$  while maintaining proper antisymmetrization. This is significant for qubit representations of fermionic operators under the Jordan-Wigner transformation, where the ordering follows a canonical sequence. This mapping fractionates  $\hat{S}_{ij}$  into multiple swap gates between adjacent qubits [34].

Under the Jordan-Wigner transformation, the corresponding qubit Hamiltonian follows canonical ordering, requiring gates between neighbouring qubits. This composite two-qubit gate defines the *fermionic simulation*

(*fSim*) gate. Explicitly:

$$\widehat{\text{fSim}} = \mathbb{P}(e^{-iC\hat{n}_i\hat{n}_{i+1}t} e^{-iA(\hat{f}_i^\dagger\hat{f}_{i+1}+h.c.)t}\hat{S}_{i,i+1}) \quad (3)$$

$A \equiv A_{i,i+1}$  and  $C \equiv C_{i,i+1}$  are the corresponding interactions between a pair of adjacent qubits.  $\mathbb{P}$  denotes the projection onto the qubit subspace defined in Eq.(2), Eq.(3) simplifies to the  $4 \times 4$  computational subspace:

$$\widehat{\text{fSim}} = \begin{pmatrix} 1 & 0 & 0 & 0 \\ 0 & -i \sin(At) & \cos(At) & 0 \\ 0 & \cos(At) & -i \sin(At) & 0 \\ 0 & 0 & 0 & -ie^{-iCt} \end{pmatrix} \quad (4)$$

Comparing Eq.(4) and Eq.(1) shows that controlling the parameters  $A$ ,  $C$ , and the gate time  $t$  are crucial for tuning the gate angles  $\varphi$  and  $\theta$ . They turn  $\theta = At - \frac{\pi}{2}$  and  $\varphi = \pi/2 - Ct$ , up to single qubit rotations.

Fig.(1) illustrates an example with four fermion states  $|\psi_1\psi_2\psi_3\psi_4\rangle$  represented by the vertical column of four qubits  $Q_a$ ,  $Q_b$ ,  $Q_c$ , and  $Q_d$  shown by circle of distinct colors. The typical fermionic state  $\psi_i$  is denoted by  $|i\rangle$  inside each circle. After four layers of *cfSim* operations, i.e. vertical dashed line, the output fermion state on the qubits will correspond to the swapped state  $|\psi_4\psi_3\psi_2\psi_1\rangle$ .

### III. CONCURRENT FERMIONIC SIMULATION GATE

In superconducting circuits consisting of two transmons coupled via a frequency-tunable coupler, a continuous two-qubit *fSim* gate has recently been realized. Individibichromatic iswap and *cphase* gates can be implemented by adjusting the qubit-qubit coupling strength and frequency detuning, with one gate activated immediately after the other is deactivated [29]. Notably, both gates can also be active simultaneously, enabling the complete and concurrent implementation of the fermionic simulation gate set in a single operation, referred to as concurrent fermionic simulation (*cfSim*). Below, we present the theory for realizing such a gate using two parametric drives in a controllable manner.

#### A. Setup: bichromatic parametric driving (BPD)

Motivated by the idea of realizing *fSim* gate by a parametric drive [36–38], in this paper, we consider the simultaneous application of two gates achieved by employing Bichromatic Parametric Driving (BPD). In this approach, we apply two parametric drives at distinct frequencies, each on one qubit. The schematic of the setup is depicted in Fig.(3). The first drive resonates the state  $|11\rangle$  with either  $|02\rangle$  or  $|20\rangle$ . The second drive facilitates a swap between the single-qubit excited states  $|10\rangle$  and  $|01\rangle$  by bringing them into resonance, as illustrated in Fig.(3). The state  $|00\rangle$  remains uncoupled from other

states because it is far detuned from the relevant transitions, thereby staying unaffected by the applied drives.

It is crucial to minimize leakage out of the computational space, which requires the state  $|11\rangle$  to complete full oscillation cycles, transferring its population out of the computational subspace (to  $|02\rangle$  or  $|20\rangle$ ) and then back. This depopulation and repopulation of  $|11\rangle$  are optimally synchronized with the swap transition between  $|01\rangle$  and  $|10\rangle$ .

The qubit dynamics of an iswap /*cphase* gate set can be efficiently modeled by two interacting qutrits with time-dependent frequency detuning  $\Delta(t) = \omega_1(t) - \omega_2(t)$  and time-dependent coupling strength  $g(t)$ . The Hamiltonian of such a system in the basis of  $|01\rangle$ ,  $|10\rangle$ ,  $|11\rangle$ ,  $|20\rangle$ ,  $|02\rangle$  from left (top) to right (bottom) is given by:

$$H_0 = \begin{pmatrix} 0 & g & 0 & 0 & 0 \\ g & \Delta & 0 & 0 & 0 \\ 0 & 0 & \Delta & \sqrt{2}g & \sqrt{2}g \\ 0 & 0 & \sqrt{2}g & 2\Delta + \delta & 0 \\ 0 & 0 & \sqrt{2}g & 0 & \delta \end{pmatrix} \quad (5)$$

with similar qutrit anharmonicity  $\delta_1 = \delta_2 \equiv \delta$  with  $\delta_i \equiv E_2^{(i)} - 2\hbar\omega_i$  denoting the anharmonicity associated to qutrit  $i$ .

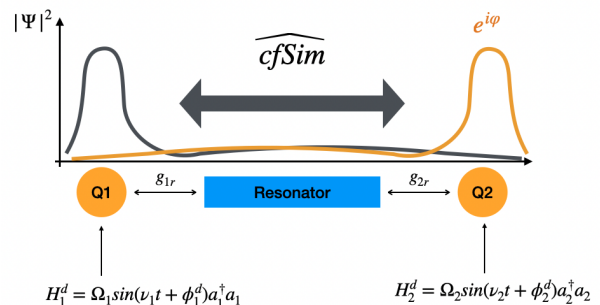


FIG. 2: Setup of the system. Two transmons are coupled via a common harmonic resonator. The direct transmon-transmon coupling is ignored. Two parametric drives are applied to the two transmons separately. There are five control parameters of the drives: two drive amplitudes  $\Omega_1$  and  $\Omega_2$ , two drive frequencies  $\nu_1$  and  $\nu_2$  and one relative phase  $\phi_1^d - \phi_2^d$ . In our analysis, the relative phase is fixed to be zero. The two simultaneous drives induce a concurrent *fSim* gate between the two qubits, exchanging their excitations and adding a conditional phase  $\varphi$ .

Our proposed gate operates by modulating the frequencies  $\omega_1$  and  $\omega_2$  in an oscillatory manner. Consider the setup depicted in Fig.(3), where both transmons  $Q_1$  and  $Q_2$ , coupled via a resonator, are parametrically driven by  $h_i(t) \equiv \Omega_i \sin(\nu_i t + \phi_i^d) \hat{a}_i^\dagger \hat{a}_i$  for  $i = 1, 2$ . Here,  $\phi_i^d$  is the driving phase,  $\nu_i$  the modulation frequency, and  $\Omega_i$  the modulation amplitude.

Since a parametric drive modifies the qubit frequency, it effectively acts as a time-dependent number operator

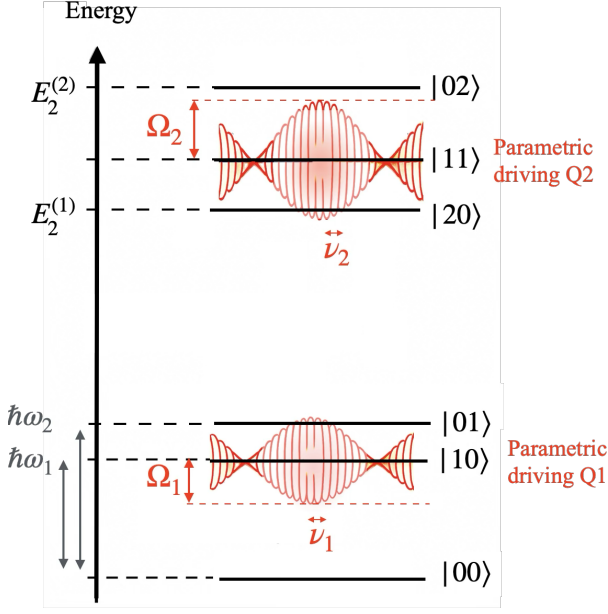


FIG. 3: Schematic of BPD for cfSim gates. Relevant levels are shown. Two parametric drives target two transitions separately. When on resonance, drive frequency  $\nu_{1,2}$  should match level detuning. Drive amplitude  $\Omega_{1,2}$  are not required to match detunings. For cfSim gates, we choose to drive 1 to resonantly drive  $|01\rangle \leftrightarrow |10\rangle$  transition, therefore,  $\nu_1 = \omega_2 - \omega_1$ . The second drive is chosen to be near resonant with  $|11\rangle \leftrightarrow |20\rangle$  or  $|11\rangle \leftrightarrow |02\rangle$  transition. iswap and cphase transitions are happening simultaneously. Both iswap angle  $\theta$  and conditional phase  $\varphi$  can be controlled.

$\hat{a}_i^\dagger \hat{a}_i$ , where  $\hat{a}_i^\dagger$  ( $\hat{a}_i$ ) represents the creation (annihilation) operator for the qutrit  $i$ . The total Hamiltonian within the  $5 \times 5$  qutrit Hilbert space of interest is expressed as:

$$H = H_0 + \begin{pmatrix} h_2(t) & 0 & 0 & 0 & 0 \\ 0 & h_1(t) & 0 & 0 & 0 \\ 0 & 0 & \sum_i h_i(t) & 0 & 0 \\ 0 & 0 & 0 & 2h_1(t) & 0 \\ 0 & 0 & 0 & 0 & 2h_2(t) \end{pmatrix} \quad (6)$$

By combining all diagonal elements into  $H_{\text{diag}}$  and transforming the Hamiltonian by the unitary matrix  $U = \exp(-i \int H_{\text{diag}}(t) dt)$  into the interaction picture — i.e.  $H_I = U^\dagger H U - iU^\dagger \frac{\partial}{\partial t} U$ ; equivalently using a rotating frame that is resonant with all levels — and simplifying the result using the Jacobi–Anger identity the total Hamiltonian is transformed into:

$$H = \sum_{m,n=0}^{\infty} g J_m \left( \frac{\Omega_1}{\nu_1} \right) J_n \left( \frac{\Omega_2}{\nu_2} \right) e^{-it(m\nu_1 + n\nu_2)} \times \\ (e^{it\Delta} |10\rangle\langle 01| + \sqrt{2} e^{it(\delta + \Delta)} |11\rangle\langle 02| \\ + \sqrt{2} e^{it(\delta - \Delta)} |11\rangle\langle 20| + H.c.) \quad (7)$$

in which  $J_n$  is the Bessel function of the first kind, and the summation takes place over integers  $n \in \mathbb{Z}$ .

Without loss of generality, let us assume that the frequency of Q1 is greater than that of Q2, i.e.  $\omega_1 > \omega_2$ . For this setup, we can parametrically drive the frequency of Q1 by supplying the required energy to achieve the transition  $|01\rangle \leftrightarrow |10\rangle$ , i.e.  $\nu_1 = \Delta$ . The second qubit Q2 is parametrically driven to come very close to the resonance between  $|11\rangle \leftrightarrow |02\rangle$  transition, i.e.  $\nu_2 = \Delta + \delta + \varepsilon$  with small  $|\varepsilon|$ , i.e.  $|\varepsilon| \ll \min\{|\Delta + \delta|, |\Delta - \delta|\}$ . By this assumption, only the slow-varying terms proportional to  $\exp(i\varepsilon t)$  contribute to the state evolution in the long run  $t \gg 1/(\Delta \pm \delta)$ . The Hamiltonian (7) contains interaction within and outside the Hilbert space’s computational subset. Within the computational subset there is exchange interaction  $|10\rangle\langle 01|$  with the strength  $gJ_1(\Omega_1/\Delta)J_0(\Omega_2/(\Delta + \delta + \varepsilon))$ . Outside of the computational subset the energy level  $|11\rangle$  interacts with  $|02\rangle$  and  $|20\rangle$  by the following coupling strength  $\sqrt{2}gJ_0(\Omega_1/\Delta)J_1(\Omega_2/(\Delta + \delta + \varepsilon))e^{i\varepsilon t}$  and  $\sqrt{2}gJ_{-2}(\Omega_1/\Delta)J_1(\Omega_2/(\Delta + \delta + \varepsilon))e^{i\varepsilon t}$ , respectively.

From here on, this analysis can be performed numerically to simulate the behavior of the two qubits under the two parametric drives, however before that, we approach the problem perturbatively.

## B. Weak BPD

It is helpful that we first consider some restrictions on the parameter domains to make the problem eligible for a valid solution in the perturbative orders.

One of the aspects of perturbatively validity of our result is that the qubits are weakly driven, therefore we consider that the drive amplitude is weak, i.e.  $\Omega_i < \nu_i$  for  $i = 1, 2$ . Within this limit which makes the arguments of the Bessel function, small, one can show that  $J_{-2}J_1 \ll J_1J_0$ ; therefore, the coupling strength of  $|11\rangle\langle 20|$  transition turns out to be negligible compared to the other two interaction strengths and can be approximately ignored. Therefore in the interaction picture after rotating-wave-approximation, the BPD Hamiltonian can be simplified as

$$H = gJ_1(x_1)J_0(x_2)|10\rangle\langle 01| \\ + \sqrt{2}gJ_0(x_1)J_1(x_2)e^{i\varepsilon t}|11\rangle\langle 02| + h.c. \quad (8)$$

The residual time dependence in the coupling between  $|11\rangle$  and  $|02\rangle$  can be treated by applying another rotating frame transformation defined as  $U_R = e^{-i\varepsilon t|02\rangle\langle 02|} \otimes I$  which rotates  $|02\rangle$  state and leaves other levels unchanged. This helps to transform the interaction to the frame rotating with the frequency of level detuning between  $|11\rangle$  and  $|02\rangle$ . The resulting Hamiltonian turns out to be block-diagonal with the following two diagonal blocks, that resemble separate iswap gates in the subspace spanned by  $|10\rangle, |01\rangle$  and cphase gate in the

subspace spanned by  $|11\rangle, |02\rangle$ , as follows:

$$H_{\text{iswap}} = \begin{pmatrix} 0 & gJ_1(x_1)J_0(x_2) \\ gJ_1(x_1)J_0(x_2) & 0 \end{pmatrix}, \quad (9)$$

$$H_{\text{cphase}} = \begin{pmatrix} 0 & \sqrt{2}gJ_0(x_1)J_1(x_2) \\ \sqrt{2}gJ_0(x_1)J_1(x_2) & -\varepsilon \end{pmatrix} \quad (10)$$

Note that in our numerical analysis we carry on the analysis in the presence of all possible transitions and therefore we consider the weak driving limit of this section only to make analysis simpler for analytical verification. Performing the analytical study in the relatively intermediate regime of driving amplitude requires to reconsider the coupling  $|11\rangle\langle 20|$  that needs to deal with  $3 \times 3$  matrix size everywhere.

We have now established that it is possible to express parametrically driven cphase and iswap operations using a 2x2 matrix representation. Consequently, we propose describing the operators for the iswap and cphase gates using an identical matrix. To facilitate this approach, we can mathematically introduce the following hypothetical Hamiltonian:

$$H = \begin{pmatrix} 0 & g \\ g & \Delta \end{pmatrix} \quad (11)$$

In the case of iswap the two columns (and rows) indicate the states  $|01\rangle$  and  $|10\rangle$  with  $g$  being the interchanging strength between the two, which is nearly the interaction strength between the two qubits in the computational level,  $\Delta$  the frequency detuning of the two qubits. Yet the very matrix of Eq.(11) can represent the cphase operator once the columns (and rows) are labelled by  $|11\rangle$  and  $|02\rangle$ . Therefore  $g$  for the cphase operator will be the interaction strength between the highest excited level in computational subspace of two qubits with the closest non-computational energy level.

Now consider that the state of two isolated qubits is evolved for a specific time  $t$  only by the unitary operator  $U(t)$ , i.e.  $U(t) = e^{-iHt}$ . In the two-level picture we chose for the two gates in Eq.(11), the unitary state evolution operator can be represented as  $U(t) = e^{-it\Delta/2} \left( \cos(\Omega t) \hat{1} - i \sin(\Omega t) \left( n_z \hat{Z} + n_x \hat{X} \right) \right)$ , with  $\hat{X}$  and  $\hat{Z}$  being the Pauli matrices, the Rabi frequency  $\Omega = \sqrt{(\Delta/2)^2 + g^2}$  determining the rotation rate. The Pauli coefficients  $n_z = -\Delta/2\Omega$  and  $n_x = g/\Omega$  define the rotation axes.

The iswap transition usually occurs by bringing the frequency of one qubit in resonance with the other qubit or applying a resonant drive with the qubit-qubit detuning. In the case of applying a resonant drive, the frequency detuning  $\Delta$  between the two qubits becomes zero in the rotating frame. In this case one can show  $|\langle 01|U(t)|10\rangle| = \sin(gt)$  which indicates the rotation iswap angle  $\theta$  can be obtained by applying the gate  $U(t)$  for certain time; i.e.  $\theta \equiv \arcsin(|\langle 01|U(t)|10\rangle|) = gt$ .

The cphase gate requires frequency detuning  $\Delta$  between the two qubits. In this gate transition sends the

photon outside of the computational level, however in order to minimize leakage, it is demanded that the final state goes back to  $|11\rangle$  at the end of the cycle of two cphase evolutions. Therefore the total evolution adds a phase to the state  $|11\rangle$ .

$$U(t_g) = -e^{-i\frac{\Delta t_g}{2}} \quad (12)$$

$$\text{with } t_g = \frac{2\pi}{\sqrt{\Delta^2 + 4g^2}}$$

So, the conditional phase  $\varphi$  is given by

$$\varphi = \pi \left( 1 - \frac{\Delta}{\sqrt{\Delta^2 + 4g^2}} \right) \quad (13)$$

In terms of  $t_g$  it can be simplified as:

$$\varphi = \pi \left( 1 - \frac{\Delta}{2\pi} t_g \right) \quad (14)$$

Therefore, the iswap angle  $\theta$  and the conditional phase  $\varphi$  can be controlled by tuning the corresponding coupling strengths and drive detuning.

Note that this is not the only way to drive a tunable conditional phase. In another approach, one drives the  $|10\rangle \leftrightarrow |02\rangle$  transition with zero detuning and stays at  $|02\rangle$  for varying time to accumulate different conditional phases[39]. The accumulated phase is given by  $\varphi = (\omega_{20} - \omega_{10} - \omega_{01})\tau$ , with  $\tau$  being the waiting time at  $|20\rangle$ . This gate can be implemented fast because  $\omega_{20} - \omega_{10} - \omega_{01}$  is usually in the hundred MHz range. The total conditional phase combines the dynamical and geometric phases in the above cases. It is also possible to have a pure geometric conditional phase by properly choosing the evolution trajectory on the Bloch sphere[40].

### C. Strong BPD

Let us once again consider the case of two flux-tunable transmons coupled via a harmonic resonator, as depicted in the hardware schematic of Fig.(2), however now we consider large Hilbert space for each transmon and coupler. Bichromatic parametric drives are applied to the device, with each drive acting on one transmon. For simplicity of analysis, we consider the setup where one drive is applied to each transmon individually. However, this is not a necessary condition from a theoretical perspective. Drives could instead be applied to the resonator, if it is also tunable, or both drives could be applied to a single transmon or the coupler.

Neglecting the counter-rotating terms, we can write down the general Hamiltonian of the system:

$$\begin{aligned}
H &= H_0 + H_d, \\
H_0 &= \sum_{\alpha=1,2,c} \omega_\alpha \hat{a}_\alpha^\dagger \hat{a}_\alpha + \frac{\delta_j}{2} \hat{a}_\alpha^\dagger \hat{a}_\alpha (\hat{a}_\alpha^\dagger \hat{a}_\alpha - 1) \\
&\quad + \sum_{j,k=\{1,2\}} g_j (\hat{a}_j^\dagger \hat{a}_c + H.c.), \\
H_d &= \sum_{j=1,2} \Omega_j \sin(\nu_j t + \phi_j^d) \hat{a}_j^\dagger \hat{a}_j.
\end{aligned} \tag{15}$$

where the subindex  $c$  denotes the coupler,  $g_j$  is the coupling strength between transmon  $j$  and the coupler. For the case of a harmonic coupler one expects that  $\delta_c = 0$ , but in general coupler can also be another qubit with non-zero anharmonicity  $\delta_c$ .

The total Hamiltonian  $H$  in Eq.(15) consists of the undriven Hamiltonian  $H_0$  and the drive Hamiltonian  $H_d$ . The undriven Hamiltonian  $H_0$  is the generalized Jaynes-Cummings Hamiltonian[41]. The drive Hamiltonian has the standard form of parametric drives[37, 42–50].

In order to accurately study the dynamics of the system, we first find a transformation  $U_0$  that diagonalizes  $H_0$ , i.e.  $\tilde{H}_0 = U_0^\dagger H_0 U_0$  with  $\tilde{H}_0$  denoting diagonalized  $H_0$ . By transforming the drive Hamiltonian to the same diagonal frame where  $H_0$  is diagonalized, the drive Hamiltonian becomes  $\tilde{H}_d = U_0^\dagger H_d U_0$ , which is not necessarily a diagonal matrix. The total Hamiltonian in the diagonal frame is then  $\tilde{H}_0 + \tilde{H}_d$ . Note that in this treatment, we are studying the dynamics in the dressed basis of the undriven Hamiltonian. Note that the diagonal transformation  $U_0$  can be analytically found using the Bogoliubov transformation[51–53] or by exact numerical diagonalization. For a derivation using the Bogoliubov transformation, see Appendix (A).

Here, in order to perform precise analysis we numerically determine the diagonalization transformation matrix  $U_0$  and compare results with what we find analytically in Appendix (A). It should be mentioned that this does not add too much computational cost when the undriven Hamiltonian  $H_0$  is fixed.

Let us denote dressed transmon states by  $Q_1$  and  $Q_2$ , and dressed coupler states with  $R$ . In the Fock basis  $\{|Q_1 Q_2 R\rangle\}$ . Total Hamiltonian reads:

$$\begin{aligned}
\tilde{H} &= \sum_{Q_1, Q_2, R} \left\{ \left( \tilde{\omega}_{Q_1, Q_2, R} + \sum_{m=1,2} \Omega_m \sin(\nu_m t + \phi_m^d) N_{Q_1, Q_2, R}^m \right) |Q_1 Q_2 R\rangle \langle Q_1 Q_2 R| \right. \\
&\quad \left. + \sum_{Q'_1, Q'_2, R'} \sum_{m=1,2} \Omega_m \sin(\nu_m t + \phi_m^d) C_{Q'_1, Q'_2, R'; Q_1, Q_2, R}^m |Q'_1 Q'_2 R'\rangle \langle Q_1 Q_2 R| \right\}
\end{aligned} \tag{16}$$

with  $\tilde{\omega}_{Q_1, Q_2, R}$ ,  $N_{Q_1, Q_2, R}^m$  and  $C_{Q'_1, Q'_2, R'; Q_1, Q_2, R}^m$  being defined as follows:

$$\begin{aligned}
\tilde{\omega}_{Q_1, Q_2, R} &= \langle Q_1 Q_2 R | \tilde{H}_0 | Q_1 Q_2 R \rangle \\
N_{Q_1, Q_2, R}^m &= \langle Q_1 Q_2 R | U_0^\dagger \hat{a}_m^\dagger \hat{a}_m U_0 | Q_1 Q_2 R \rangle \\
C_{Q'_1, Q'_2, R'; Q_1, Q_2, R}^m &= \langle Q'_1 Q'_2 R' | U_0^\dagger \hat{a}_m^\dagger \hat{a}_m U_0 | Q_1 Q_2 R \rangle
\end{aligned} \tag{17}$$

defining  $\tilde{\omega}_{Q_1, Q_2, R}$  as the eigenfrequency of the dressed state  $|Q_1 Q_2 R\rangle$ . The transformed operator  $U_0^\dagger \hat{a}_m^\dagger \hat{a}_m U_0$  is split into the diagonal term  $N_{Q_1, Q_2, R}^m$  and the off-diagonal term  $C_{Q'_1, Q'_2, R'; Q_1, Q_2, R}^m$ . The two parametric drives of BPD are denoted by  $\Omega_m \sin(\nu_m t + \phi_m^d)$  modulates the eigenfrequencies of the dressed state  $|Q_1 Q_2 R\rangle$  through the diagonal term  $N_{Q_1, Q_2, R}^m$ . These drives also introduces time dependent coupling between  $|Q_1 Q_2 R\rangle$  and  $|Q'_1 Q'_2 R'\rangle$  via the off-diagonal term  $C_{Q'_1, Q'_2, R'; Q_1, Q_2, R}^m$ .

We define the rotating frame corresponding to the di-

agonal part of  $\tilde{H}$ :

$$\begin{aligned}
U_r &= e^{-i \int dt \sum_{Q_1, Q_2, R} |Q_1 Q_2 R\rangle \langle Q_1 Q_2 R | \tilde{H} | Q_1 Q_2 R\rangle \langle Q_1 Q_2 R|} \\
&= \sum_{Q_1, Q_2, R} e^{-i \int \langle Q_1 Q_2 R | \tilde{H} | Q_1 Q_2 R \rangle dt} |Q_1 Q_2 R\rangle \langle Q_1 Q_2 R|
\end{aligned} \tag{18}$$

We transform the Hamiltonian in to the rotating frame  $\tilde{H}_R = U_r^\dagger \tilde{H} U_r - i U_r^\dagger \partial_t U_r$  and simplify to find:

$$\tilde{H}_R = \sum \tilde{G}(t)_{Q_1, Q_2, R; Q'_1, Q'_2, R'} |Q'_1 Q'_2 R'\rangle \langle Q_1 Q_2 R| \tag{19}$$

For the full derivation and the expression of  $\tilde{G}(t)_{Q_1, Q_2, R; Q'_1, Q'_2, R'}$  see Appendix (B).

### 1. Monochromatic parametric driving case

Let us consider the simple and special case of single parametric driving, namely ‘Monochromatic Parametric Drive (MPD).’ We apply MPD to Q1 to evaluate the time-dependency of the coupling strength between the

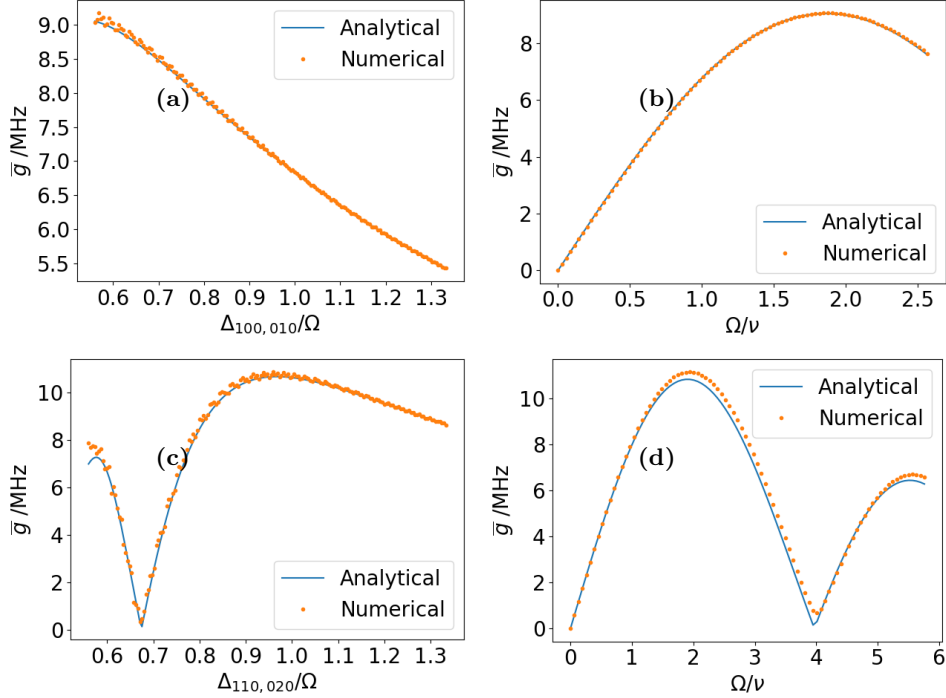


FIG. 4: Static coupling strength, analytical and numerical. We show results from the exact diagonalization method and full numerical simulation. The analytical formula is valid for a wide range, from dispersive regimes to strong coupling regimes. 4(a) Static  $\bar{g}_{100,010}$  vs qubit detuning. 4(b) Static  $\bar{g}_{100,010}$  vs drive amplitude. 4(c) Static  $\bar{g}_{110,020}$  vs qubit detuning. The dip around 300 MHz corresponds to the root of  $J_0(x) + J_2(x)$ . 4(d) Static  $\bar{g}_{110,020}$  vs drive amplitude. The analytical formula can well capture non-linear dependence on  $\Omega$ .

swap between transmons,  $|010\rangle \leftrightarrow |100\rangle$ . The drive frequency is resonant with the transition:  $\nu_1 = |\tilde{\omega}_{010} - \tilde{\omega}_{100}|$ .

In Appendix (B) we generalize the case where transmons and coupler are flux-tunable and we apply three parametric drives, two on qubits with frequencies  $\nu_1$  and  $\nu_2$ , and one with frequency  $\nu_0$  on the coupler. For this general case we worked out the resonant condition for transition  $|Q_1 Q_2 R\rangle \leftrightarrow |Q'_1 Q'_2 R'\rangle$  will be  $\tilde{\omega}_{Q'_1 Q'_2 R'} - \tilde{\omega}_{Q_1 Q_2 R} - (n_0 \nu_0 + n_1 \nu_1 + n_2 \nu_2) = 0$  with integer numbers  $n_0$ ,  $n_1$ , and  $n_2$ . The general resonance condition includes multi-photon processes, which indicates the presence of subharmonic interactions, see [54]. This condition for the case of MPD is simplified to the condition with  $\nu_0 = \nu_2 = 0$ .

If there is a dominant slow-oscillating component in  $G(t)$ , this term primarily governs the dynamics of the corresponding transition. Consequently, one can apply the Rotating Wave Approximation (RWA) by disregarding all other fast-oscillating terms.

For MPD under the resonant condition the static coupling strength between  $|100\rangle$  and  $|010\rangle$  can be determined as follows:

$$\bar{g}_{100,010} = i\alpha\Omega_1 \left[ J_2 \left( \frac{\beta\Omega_1}{\nu_1} \right) + J_0 \left( \frac{\beta\Omega_1}{\nu_1} \right) \right] \quad (20)$$

where we define  $\alpha \equiv C_{100,010}^1/2$ ,  $\beta \equiv N_{100}^1 - N_{010}^1$ .

The coupling strength between  $|110\rangle$  and  $|020\rangle$  can be

calculated similarly when the drive frequency  $\nu_1$  is resonant with  $\Delta_{110,020} = \tilde{\omega}_{110} - \tilde{\omega}_{020}$ , see Appendix (B).

The formula Eq.(20) is valid across a wide range, from the dispersive regime to the strong coupling/drive regime, as no perturbative expansion is employed in its derivation. The only approximation utilized is the RWA. The parameters  $\alpha$  and  $\beta$  are determined by the underlying undriven Hamiltonian and are obtained through exact numerical diagonalization of this Hamiltonian. As a result, our findings are exact with respect to the bare frequencies and bare couplings.

The first term,  $\alpha\Omega_1$ , represents the dominant linear dependence of  $g_{010,100}$  on  $\Omega_1$ . The constant  $\alpha$  is proportional to the coupling coefficient  $C_{100,010}^1$ . This result naturally arises from the Hamiltonian (16), where the term associated with  $C_{100,010}^1$  is the only static coupling between  $|100\rangle$  and  $|010\rangle$ . Consequently, the leading linear coupling is given by  $\alpha\Omega_1$ .

The second term,  $J_2(\beta\Omega_1/\nu_1) + J_0(\beta\Omega_1/\nu_1)$ , introduces nonlinearity to  $g_{010,100}$ . This nonlinearity arises from the modulation of the frequencies of the dressed states  $|100\rangle$  and  $|010\rangle$  induced by the parametric drives. The argument of the Bessel functions,  $\beta\Omega_1/\nu_1$ , consists of three components:

1.  $\beta$ : Reflects how differently the drives are coupled to the states  $|100\rangle$  and  $|010\rangle$ , given by the difference of the diagonal terms  $N_{100}^1 - N_{010}^1$ .

2. Drive amplitude  $\Omega_1$  (numerator): Determines the drive strength. A stronger drive results in a more significant nonlinear effect.
3. Drive frequency  $\nu_1$  (denominator): Indicates how rapidly the drive modulates the frequencies of the states. Faster modulation reduces the nonlinearity.

This nonlinear contribution is typically absent in perturbative treatments but can become significant when the drive amplitude is comparable to the drive frequency.

We calculate the static coupling strengths  $g_{010,100}$  and  $g_{110,020}$  under their respective resonant drives ( $\nu_1 = \Delta_{010,100}$  and  $\nu_1 = \Delta_{110,020}$ ) and compare the results with numerical simulations in Fig. (4). The nonlinear behavior is well captured by the analytical formulas. The transition  $g_{110,020}$  exhibits more pronounced nonlinearity because the transition frequency  $\Delta_{110,020}$  is smaller, leading to a larger ratio  $\Omega/\nu$ .

The dips observed in Fig. (4 c) and Fig. (4 d) correspond to the condition  $J_2(\beta\Omega_1/\nu_1) + J_0(\beta\Omega_1/\nu_1) = 0$ , which results in  $g_{110,020} = 0$ . Solving the equation  $J_2(\beta\Omega_1/\nu_1) + J_0(\beta\Omega_1/\nu_1) = 0$  numerically yields the root  $\beta\Omega_1/\nu_1 \approx 3.83$ , which matches well with the numerical simulation.

#### IV. CROSSTALK IN BPD

For the case of BPD with two parametric drives, the static coupling strength  $g$  between two states can be evaluated similarly. For instance, the static coupling between  $|010\rangle$  and  $|100\rangle$  under one resonance drive  $\Omega_1 \sin(\nu_1 t) a_1^\dagger a_1$  and one off-resonant drive  $\Omega_2 \sin(\nu_2 t) a_2^\dagger a_2$  is given by:

$$\bar{g}_{100,010} = i\alpha\Omega_1 \left[ J_2 \left( \frac{\beta\Omega_1}{\nu_1} \right) + J_0 \left( \frac{\beta\Omega_1}{\nu_1} \right) \right] J_0 \left( \frac{\gamma\Omega_2}{\nu_2} \right) \quad (21)$$

where

$$\alpha = \frac{C_{100,010}^1}{2}, \beta = N_{100}^1 - N_{010}^1, \gamma = N_{100}^2 - N_{010}^2 \quad (22)$$

Details of derivation and even more general case of three parametric drives can be found in Appendix (B).

The first part of  $\bar{g}_{100,010}$ ,  $i\alpha\Omega_1(J_2(\beta\Omega_1/\nu_1) + J_0(\beta\Omega_1/\nu_1))$ , is identical to the static  $\bar{g}_{100,010}$  derived under a single resonant drive, as shown in Eq. (20). The crosstalk effect of the off-resonant drive is introduced through the last term,  $J_0(\gamma\Omega_2/\nu_2)$ . This term takes a similar form to the nonlinear term in the single-drive case. The crosstalk arises from the frequency modulation of the states  $|100\rangle$  and  $|010\rangle$  induced by the second drive.

The crosstalk factor has two key features:

1. Nonlinearity: The crosstalk appears through the nonlinear function  $J_0$ .
2. Dependence on the ratio  $\Omega_2/\nu_2$ : The crosstalk depends solely on this ratio.

For small values of  $\Omega_2/\nu_2$ ,  $J_0$  is a monotonically increasing function. As  $\Omega_2/\nu_2$  increases,  $J_0$  begins to oscillate around zero, resulting in multiple zeros in  $\bar{g}_{100,010}$  and  $P_{100}$ . This behavior is illustrated in Fig. (5) and Fig. (12) in Appendix (C).

The crosstalk can be understood as an off-resonant baseband modulation on top of a resonant sideband transition. The resulting coupling strength is the product of the two parts. Eq.(21) can be generalized to N drives, where only one drive is resonant and all other N-1 drives are off-resonant:

$$\bar{g} = i\alpha\Omega_1 \left( J_2 \left( \beta \frac{\Omega_1}{\nu_1} \right) + J_0 \left( \beta \frac{\Omega_1}{\nu_1} \right) \right) \prod_{k=2}^N J_0 \left( \gamma_k \frac{\Omega_k}{\nu_k} \right) \quad (23)$$

Our result Eq.(23) also applies to multi-qubit systems. One can use it to suppress a target transition by requiring  $\prod_{k=2}^N J_0 \left( \gamma_k \frac{\Omega_k}{\nu_k} \right) = 0$ .

#### V. OPTIMIZATION AND RESULTS

Driving the cphase transition while the iswap drive is present needs more delicate treatment because we require the state always to return to  $|11\rangle$  at the end of the gate with a fixed gate time  $t_g$ . When one of the drives is far-detuned,  $|\Delta_{110,020} - \nu_1| \gg \Delta_{110,020}$ , and the other is near-resonant  $|\Delta_{110,020} - \nu_2| \ll \Delta_{110,020}$ . The first order coupling strength between  $|110\rangle$  and  $|020\rangle$  is:

$$\tilde{G}_{110,020}^{\text{eff}} = i\alpha\Omega_2 J_0 \left( \frac{\beta\Omega_1}{\nu_1} \right) \left[ J_2 \left( \frac{\gamma\Omega_2}{\nu_2} \right) + J_0 \left( \frac{\gamma\Omega_2}{\nu_2} \right) \right] \times \exp \left( i(\tilde{\Delta}_{110,020} - \nu_2)t \right) \quad (24)$$

with the following definitions:

$$\alpha = \frac{C_{110,020}^2}{2}, \beta = N_{110}^1 - N_{020}^1, \gamma = N_{110}^2 - N_{020}^2 \quad (25)$$

Within the space of acting cphase, which are  $\{|110\rangle, |020\rangle\}$  subspace, we can define the following Pauli operators:

$$\begin{aligned} \hat{\Sigma}^+ &= |020\rangle\langle 110|, \quad \hat{\Sigma}^- = |110\rangle\langle 020| \\ \hat{\Sigma}^z &= |110\rangle\langle 110| - |110\rangle\langle 020| \\ \hat{\Sigma}^x &= |020\rangle\langle 110| + |110\rangle\langle 020| \end{aligned} \quad (26)$$

The effective Hamiltonian in this subspace which then can be written as:

$$H = ig\hat{\Sigma}^+ e^{i\Delta t} + H.c. \quad (27)$$



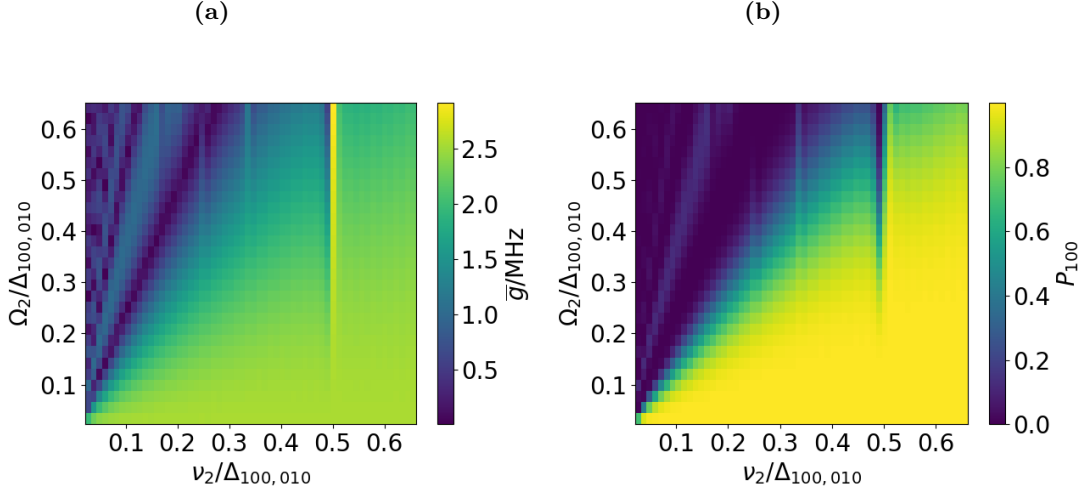


FIG. 5: Crosstalk effect of one drive on the other. (a) Numerical simulation of static  $\bar{g}_{100,010}$  vs  $\Omega_2$  and  $\nu_2$  while the first drive is fixed at  $\Omega_1 = 150$  MHz,  $\nu_1 = \Delta_{010,100}$ , which is far detuned from  $|010\rangle \leftrightarrow |100\rangle$  transition. Only the first drive is in resonance. The static coupling  $\bar{g}_{100,010}$  is modulated by the second parametric drive. The dark stripes correspond to zeros of  $J_0$  at  $\Omega_2/\nu_2 = 2.40, 5.52, 8.65, \dots$ . The pattern is consistent with analytical calculation and Fig.(12). The anomalous resonance around  $\nu_2 = 225$  MHz is not captured by RWA formula, because at this spot  $2\nu_2 = \Delta_{010,100}$  and 2-photon transition needs to be included to account for this resonance. (b) Numerical simulation of  $P_{100}$  is consistent with analytical result except for 2-photon transition, see Fig.(12).

with the definition of  $g$  as follows:

$$\begin{aligned} \Delta &= \Delta_{110,020} - \nu_2 \\ g &= \alpha\Omega_2 J_0\left(\frac{\beta\Omega_1}{\nu_1}\right) \left( J_2\left(\frac{\gamma\Omega_2}{\nu_2}\right) + J_0\left(\frac{\gamma\Omega_2}{\nu_2}\right) \right) \end{aligned} \quad (28)$$

We can now make another rotating frame transformation  $U_r = \exp[-i(\Delta t + \pi/2)\hat{\Sigma}^z/2]$  to rotate away the time-dependent factor  $ie^{i\Delta t}$ . The transformed Hamiltonian is given by :

$$\begin{aligned} \tilde{H} &= U_r^\dagger H U_r - iU_r^\dagger \frac{\partial U_r}{\partial t} \\ &= \frac{\Delta}{2}\hat{\Sigma}^z + g\hat{\Sigma}^x \end{aligned} \quad (29)$$

The time evolution can now easily be calculated:

$$\begin{aligned} U(t) &= e^{-i\tilde{H}t} \\ &= \cos(\Omega t)\hat{I} - i\sin(\Omega t)(n_z\hat{\Sigma}^z + n_x\hat{\Sigma}^x) \end{aligned} \quad (30)$$

where  $\Omega = \sqrt{(\frac{\Delta}{2})^2 + g^2}$ ,  $n_z = \Delta/\sqrt{\Delta^2 + 4g^2}$  and  $n_x = 2g/\sqrt{\Delta^2 + 4g^2}$ . Note that a part of conditional phase due to ZZ interaction is now absorbed in the rotating frame transformation  $U_r$  [55].

To maintain a constant gate time  $t_g$ , we require:

$$\begin{aligned} \Omega t_g &= \pi \\ \Rightarrow g &= \pm \sqrt{\left(\frac{\pi}{t_g}\right)^2 - \left(\frac{\Delta}{2}\right)^2} \end{aligned} \quad (31)$$

Now combining Eq.(28) and Eq.(31), we can numerically solve for the optimal amplitude of the second drive  $\Omega_2$  for a given set of  $(t_g, \nu_1, \Omega_1, \nu_2)$ :

$$\alpha\Omega_2 J_0\left(\beta\frac{\Omega_1}{\nu_1}\right) \left( J_2\left(\gamma\frac{\Omega_2}{\nu_2}\right) + J_0\left(\gamma\frac{\Omega_2}{\nu_2}\right) \right) = \pm \sqrt{\left(\frac{\pi}{t_g}\right)^2 - \left(\frac{\Delta_{110,020} - \nu_2}{2}\right)^2} \quad (32)$$

Eq.(32) is the main equation that we need for determining the optimal amplitude of the second drive. Note that once  $\alpha, \beta$  and  $\gamma$  are fixed in Eq.(28) by a given undriven Hamiltonian, the sign of  $g$  normally won't change

within a reasonable range of  $\frac{\nu_{1,2}}{\Omega_{1,2}}$  unless we flip the signs of  $\Omega_{1,2}$  or  $\nu_{1,2}$ . So we will only see a single branch in the numerical solution of  $g$ . The optimal amplitude shows up as a low-leakage trajectory around a high-leakage cen-

ter in the 2D scan of  $\nu_2$  and  $\Omega_2$ . Following the trajectory we have the lowest leakage (complete cycle of  $|110\rangle \rightarrow |020\rangle \rightarrow |110\rangle$ ) and also tunable cphase, see FIG.6.

The analytical formula Eq.(32) can accurately predict the optimal drive amplitude  $\Omega_2$ , Fig.(7). The curve for optimal  $\Omega_2$  has the shape of a semi-ellipse. In fact, up to first order approximation, Eq.(32) becomes  $(\alpha J_0(\beta \frac{\Omega_1}{\nu_1})\Omega_2)^2 + (\frac{\Delta_{110,020}-\nu_2}{2})^2 = (\frac{\pi}{t_g})^2$ , which defines an elliptic curve. We also notice that for a given  $\nu_2$ , a larger  $\Omega_1$  requires a larger  $\Omega_2$ , see Fig. (7 b). This is because for a given  $\nu_2$  the target  $g$  is fixed, see Eq.(31). However, due to the crosstalk effect of the first drive, one needs to increase  $\Omega_2$  to compensate for the modulation factor  $J_0(\beta \frac{\Omega_1}{\nu_1})$ . This is consistent with the result in Fig. (12).

## VI. CONCURRENCY IN THE CFSIM GATE

Combining the results above, we can now write down the equations for the iswap angle  $\theta$  and conditional phase  $\varphi$  including the contribution from ZZ interaction and the constraint condition for  $\Omega_2$  for a given set of  $(t_g, \Omega_1, \nu_2)$  with  $\nu_1 = \Delta_{100,010}$ :

$$\begin{aligned} \sin(\theta) &= \frac{1 - \cos(2g_1 t_g)}{2} \\ \varphi &= \pi \left( 1 - \frac{\Delta_{110,020} - \nu_2 + 2\xi_{zz} t_g}{2\pi} \right) \\ g_2 &= \pm \sqrt{\left(\frac{\pi}{t_g}\right)^2 - \left(\frac{\Delta_{110,020} - \nu_2}{2}\right)^2} \end{aligned} \quad (33)$$

with

$$\begin{aligned} g_1 &= \alpha_1 \Omega_1 \left( J_2 \left( \beta_1 \frac{\Omega_1}{\nu_1} \right) + J_0 \left( \beta_1 \frac{\Omega_1}{\nu_1} \right) \right) J_0 \left( \gamma_1 \frac{\Omega_2}{\nu_2} \right) \\ g_2 &= \alpha_2 \Omega_2 J_0 \left( \beta_2 \frac{\Omega_1}{\nu_1} \right) \left( J_2 \left( \gamma_2 \frac{\Omega_2}{\nu_2} \right) + J_0 \left( \gamma_2 \frac{\Omega_2}{\nu_2} \right) \right) \end{aligned} \quad (34)$$

where  $\alpha_{1,2}, \beta_{1,2}, \gamma_{1,2}$  are constants given by the underlying undriven Hamiltonian, see Eq.(22) and Eq.(25).  $\xi_{zz}$  is the ZZ interaction strength given by:

$$\xi_{zz} = E_{110} + E_{000} - E_{100} - E_{010} \quad (35)$$

In the numerical simulation, we use the following parameters from Ref.[56]:

$$\begin{aligned} \omega_1/2\pi &= 7.15 \text{ GHz}, \quad \omega_2/2\pi = 7.6 \text{ GHz}, \\ \omega_r/2\pi &= 8.1 \text{ GHz} \\ \delta_1/2\pi &= \delta_2/2\pi = -200 \text{ MHz}, \quad \delta_r = 0 \\ g_{1r}/2\pi &= g_{2r}/2\pi = 120 \text{ MHz}, \quad g_{12} = 0 \\ \phi_1^d &= \phi_2^d = 0 \\ t_g &= 100 \text{ ns} \end{aligned} \quad (36)$$

We first calculate the optimal drive amplitude  $\Omega_2$  according to Eq.(32), see Fig. (13 a) in Appendix (D). We then use the analytically calculated  $\Omega_2$  in the time-dependent Schrödinger equation and numerically solve the equation. Fig. (13 c) shows the leakage at the end of the gate. Within the valid area of Eq.(32), the leakage is suppressed below 1%. Note that in Eq.(35) we have assumed that the coupler  $|R\rangle$  is in the ground state. This is valid because the coupler is far detuned from both qubits by more than 1 GHz. During the gate, no drive is resonant with any coupler excitation. So the coupler won't be occupied during the gate execution. In Fig. (8), we plot the iswap angle  $\theta$  and conditional phase  $\varphi$  from numerical simulation and compare it to analytical results from Eq.(33).  $\theta$  is tunable from 0 to 90° and  $\varphi$  is tunable from -180° to 180°. Both can be faithfully predicted by the analytical formulas. To quantify the effect of leakage, we calculate the gate fidelity using the formula[57]:

$$F(U, U_0) = \frac{\text{Tr}(MM^\dagger) + |\text{Tr}(M)|^2}{d(d+1)} \quad (37)$$

where  $M = PU_0UP$ .  $U$  is the unitary operator of the gate process.  $U_0$  is the ideal gate operator.  $P$  is the projection operator onto the computational subspace spanned by  $\{|000\rangle, |100\rangle, |010\rangle, |110\rangle\}$  and  $d$  is the dimension of  $U$ .

The fidelity from the numerical simulation is shown in Fig. (9 a). In the fSim gate range, the fidelity is consistently above 99.5%. In most area it's above 99.9%. The cross-talk effect can be clearly seen in the line cuts Fig. (9 c). The gate fidelity is lower when  $\Omega_1$  is larger. This is most likely because of the beyond-RWA effect, which is left for future study.

The gate fidelity can be further improved by including pulse-shaping. Here we choose to use flat-top Gaussian to demonstrate the effect of pulse-shaping. One crucial step in our numerical simulation is to find the optimal drive amplitude  $\Omega_2$ , see Eq.(33) and Eq.(34). This was calculated by using RWA when the drives are rectangular pulses. In the case of pulse-shaping, however, the RWA result is inaccurate because of the slow-changing rise-and-fall edges, especially when one wants to achieve high gate fidelity. In order to overcome this problem, we choose to make a two-level approximation and numerically optimize the drive amplitude in the effective two-level system, which is spanned by  $|110\rangle$  and  $|020\rangle$  in our case. One can also include more relevant levels accordingly. During the numerical optimization, only the pulse amplitude is varied. Other parameters, such as pulse width and rise-and-fall time, are fixed, which can also affect the gate fidelity. The pulse envelop to be optimized is therefore expressed as:

$$e(t) = \Gamma f(t) \quad (38)$$

$e(t)$  is the final pulse envelop and  $f(t)$  is the standard flat top Gaussian envelop.  $\Gamma$  is the parameter to

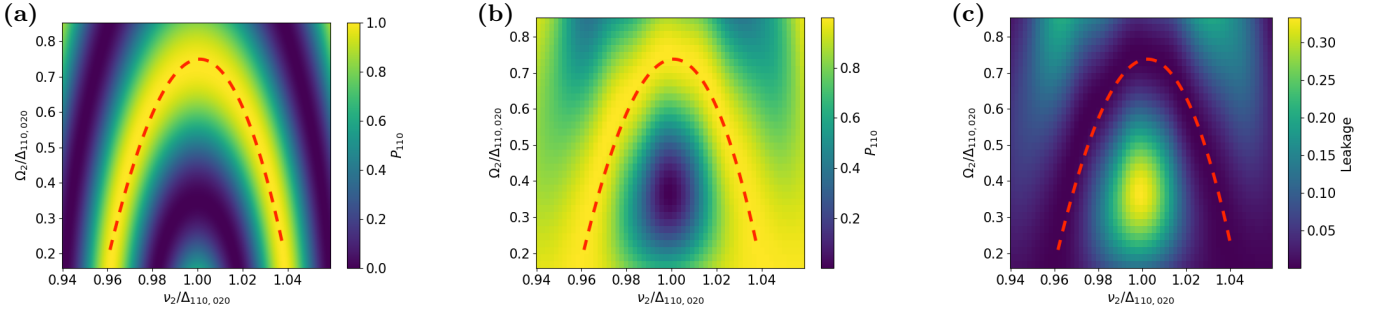


FIG. 6: Identify the optimal amplitude trajectory. The optimal trajectory is marked by the red dash line. (a) Analytical plot of P11 vs  $\Omega_2$  and  $\nu_2$  while the first drive is resonant with  $|01\rangle \leftrightarrow |10\rangle$  transition:  $\Omega_1 = 150$  MHz,  $\nu_1 = \Delta_{01,10}$ . The optimal drive amplitude  $\Omega_2$  is defined as such that P11 is maximum. (b) Numerical plot of P11 vs  $\Omega_2$  and  $\nu_2$ . It is consistent with the analytical plot. (c) Numerical plot of leakage vs  $\Omega_2$  and  $\nu_2$ . We calculate the average leakage out of the computational subspace when the initial states are  $|010\rangle$ ,  $|100\rangle$  and  $|110\rangle$ . The optimal drive amplitude  $\Omega_2$  can also be defined as such to minimize the leakage.

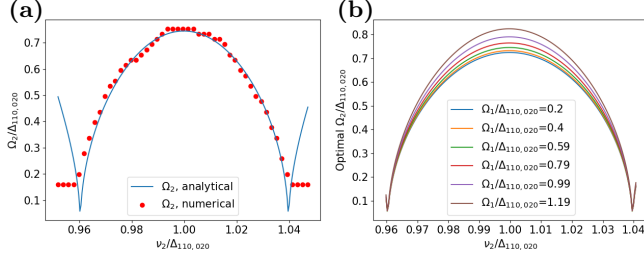


FIG. 7: Optimal  $\Omega_2$  vs  $\nu_2$ . 7(a) numerically determined optimal drive amplitude  $\Omega_2$  by minimizing leakage and analytical optimal  $\Omega_2$ . The discrepancy on the edges is because  $|\nu_2 - \Delta_{110,020}| > \frac{2\pi}{t_g}$ . No valid solution of effective coupling  $g_{110,020}$  can be found to satisfy the condition that one and only one cycle of  $|110\rangle \rightarrow |020\rangle \rightarrow |110\rangle$  is completed in the given gate time  $t_g$ . Therefore, only the  $\nu_2$  and  $\Omega_2$  in the middle area are relevant. 7(b) Analytically calculated optimal  $\Omega_2$  vs  $\nu_2$  with various  $\Omega_1$ .

be optimized. We find the optimal drive amplitude by requiring minimal leakage to  $|020\rangle$ , or equivalently maximal  $|110\rangle$  occupation. The gate fidelity, iswap probability P10 and the conditional phase with pulse-shaping are shown in Fig. (14) in Appendix (E). We can see that the gate fidelity is improved by approximately one-order-of-magnitude. The iswap and cphase patterns are roughly unchanged. To illustrate the enhancement to fidelity, we show three specific fidelity trajectories versus  $\nu_2$  in Fig. (10).

Nevertheless, we do find more discontinuities/jumps in the plots. This is because of the numerical optimization. During the optimization, especially when the drive frequency  $\nu_2$  is approaching the boundaries of the valid area of fSim gates, the resulting optimization factors may not be continuous in contrast to the analytical formulas Eq.(33) and Eq.(34) used when there is no pulse-shaping. The discontinuities in the optimization factor can be seen

clearly in Fig. (14) in Appendix (E).

We notice that the cphase gate can also be driven by multi-photon processes. According to Eq.(B10), any transition defined by  $\Delta_{110,\eta} - n_0\nu_0 - n_1\nu_1 - z\nu_2 = 0$  can be used to implement the conditional phase, where  $\eta$  denotes an ancillary level.

## VII. ZZ-FREE ISWAP IN THE CFSIM

As an example of the concurrent fSim gate, we show how to implement a  $90^\circ$  iswap gate with zero ZZ phase. We first solve for  $(\nu_2, \Omega_1, \Omega_2)$  needed to achieve  $\theta = 90^\circ, \varphi = 0$ . In fact, once  $\theta, \varphi$  are given, one can analytically solve for  $g_1, g_2$  and  $\nu_2$  using Eq.(33). We first notice that  $\theta$  is only dependent on  $g_1$ . The conditional phase  $\varphi$  and  $g_2$  are both only dependent on  $\nu_2$ . We can, therefore, first invert the expressions of  $\theta$  and  $\varphi$ . After having  $\nu_2$  expressed as a function of  $\varphi$ , we can substitute it into the expression of  $g_2$  to get the equation between  $g_2$  and  $\varphi$ . The resulting equations are:

$$\begin{aligned}
 g_1 &= \frac{\arccos(1 - 2 \sin \theta)}{2t_g} \\
 \nu_2 &= \Delta_{110,020} - 2\left(\frac{\pi - \varphi}{t_g} - \xi_{zz}\right) \\
 g_2 &= \pm \sqrt{\left(\frac{\pi}{t_g}\right)^2 - \left(\frac{\pi - \varphi}{t_g} - \xi_{zz}\right)^2}
 \end{aligned} \tag{39}$$

Therefore, one only needs to numerically solve Eq.(34) for  $(\Omega_1, \Omega_2)$ . In Fig. (11), we show the real-time evolution of the system. The target angles,  $\theta = 90^\circ, \varphi = 0$  are achieved at the end of the gate. We notice that there is a bit of over-rotation in  $P_{110}$  and  $P_{020}$ . This is because of the beyond-RWA effect. It can be corrected by including fast oscillating terms in Eq.(B8).

When the qubit is in idle mode, one can use the same method to eliminate ZZ phase. Assuming a far-off-

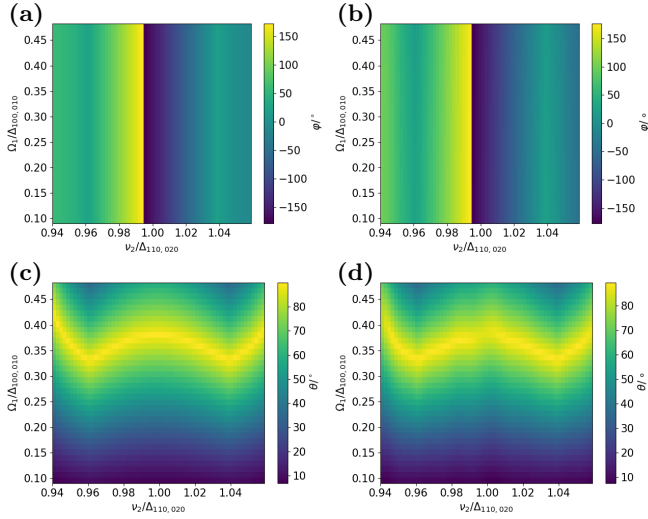


FIG. 8: Continuous fSim gate. Both  $\theta$  and  $\varphi$  are continuously tunable. 8(a) Analytically calculated conditional phase vs  $\Omega_1$  and  $\nu_2$ . The phase covers the full  $2\pi$  range from  $-\pi$  to  $\pi$ . The phase is dominantly determined by  $\nu_2$ . The vertical cut in the middle is because the range is chosen to be  $[-\pi, \pi)$  in order to manifest the zero conditional phase trajectory. Along the vertical line  $\varphi = \pi(-\pi)$ . 8(b) Numerically calculated conditional phase vs  $\Omega_1$  and  $\nu_2$ . It agrees with the analytical plot well. 8(c) Analytically calculated iswap angle  $\theta$  vs  $\Omega_1$  and  $\nu_2$ .  $\theta$  is tunable from 0 to  $90^\circ$ .  $\theta$  is mainly controlled by  $\Omega_1$  with some modulation from  $\nu_2$ . A larger  $\Omega_1$  is needed to achieve maximum  $\theta$  when  $\nu_2$  is resonant with  $\Delta_{110,020}$ . This is because when  $\nu_2$  gets closer to  $\Delta_{110,020}$ , the corresponding optimal  $\Omega_2$  becomes larger, which in turn makes  $\frac{\Omega_2}{\nu_2}$  larger. The effective coupling  $g_{010,100}$  is thus reduced, see Eq.(21) and Fig.(12). 8(d) Numerically calculated iswap angle  $\theta$  vs  $\Omega_1$  and  $\nu_2$ , consistent with analytical plot.

resonant drive  $\Omega \sin(\nu t)$ . The oscillation period is given by  $t_g = \frac{2\pi}{\sqrt{\Delta^2 + 4g^2}}$ , where  $\Delta = \Delta_{110,020} - \nu$ . The accumulated phase is  $\varphi = \pi(1 - \frac{\Delta}{\sqrt{\Delta^2 + 4g^2}}) - \xi_{zz}t_g$ . Requiring  $\varphi = 0$  we arrive at:

$$g^2 - \xi_{zz}\Delta = \frac{\xi_{zz}^2}{4} \quad (40)$$

One can numerically solve Eq.(40) by combining  $g = \alpha\Omega*(J_2(\beta\frac{\Omega}{\nu}) + J_0(\beta\frac{\Omega}{\nu}))$ . Our method, in this case, can be applied to cancel static ZZ crosstalk in superconducting quantum processors.

## VIII. SUMMARY

In summary, we presented a proposal of implementing the continuous fSim gate in superconducting sys-

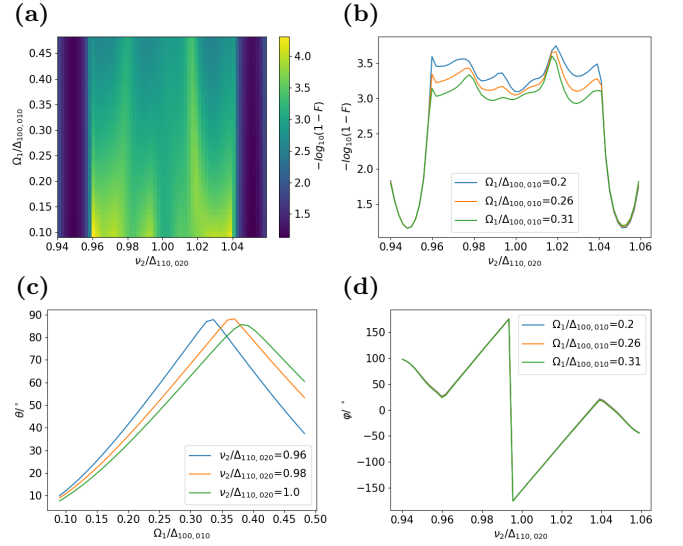


FIG. 9: 9(a) Fidelity of the fSim gate. The dark area is out of the fSim gate range. Within the fSim gate range, the fidelity is around or above 99.9%. 9(b) Fidelity along the  $\nu_2$  axis while  $\Omega_1$  is fixed. Three line cuts are shown. The fidelity domain are between 99.9% to 99.99% subject to qubit decoherence. 9(c) iswap angle  $\theta$  vs  $\Omega_1$  while  $\nu_2$  is fixed. 9(d) Conditional phase  $\varphi$  vs  $\nu_2$  while  $\Omega_1$  is fixed. The crosstalk effect on the conditional phase is small.

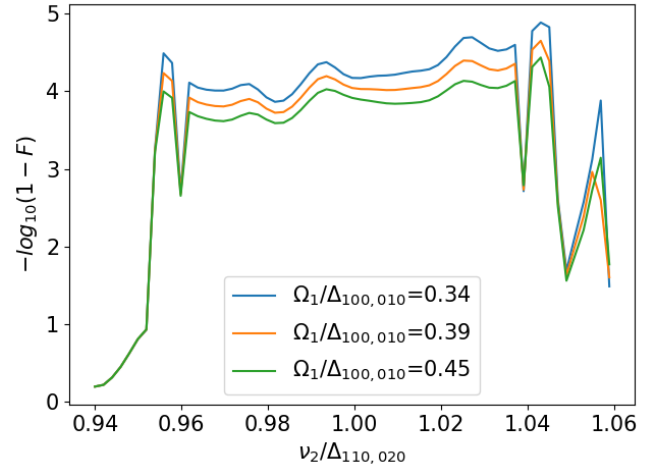


FIG. 10: Three specific line cuts of fidelities along the  $\nu_2$  axis.

tems using bichromatic parametric drives. We propose to drive the iswap transition and cphase transition simultaneously. In order to study the crosstalk effect between the two drives, we derived accurate analytical formulas of the effective coupling strength valid for a wide range: from weak coupling to strong coupling and from weak drive to strong drive. With the help of our analytical formulas, we can calculate the optimal drive amplitude

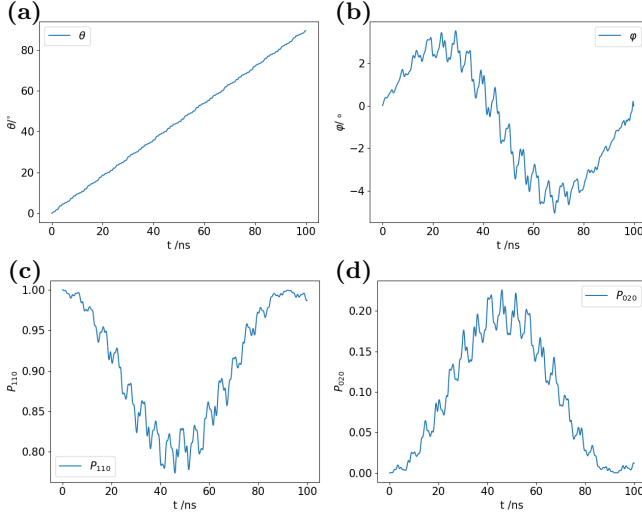


FIG. 11: An example showing pure iswap gate (conditional phase  $\varphi = 0$ ). Here we choose full iswap  $\theta = 90^\circ$ . Fidelity= 99.67%. **11(a)** real-time evolution of iswap angle  $\theta$ . **11(b)** Dynamics of conditional phase. It is governed by both the ZZ interaction and geometric phase. The overall phase is zero at the end of the gate. **11(c)** Evolution of  $P_{110}$ . It corresponds to a closed trajectory in the Bloch sphere. There is a bit of over-rotation which causes leakage. This is because we used rotating wave approximation in the analytical formula. This over-rotation can be corrected by including higher-order oscillating terms. **11(d)** Evolution of  $P_{020}$ . There is some residual population at the end of the evolution.

for minimizing leakage. The analytical calculation shows both iswap angle  $\theta$  and conditional phase  $\varphi$  can be tuned in full range, which is verified by numerical simulation. The flexibility of continuous fSim gates makes it advantageous to many quantum algorithms such as for simulating fermionic systems. The gate protocol is applicable to current superconducting quantum computation platforms. We hope it can facilitate the practical application of quantum computation in the NISQ era.

## ACKNOWLEDGMENTS

The authors thank Rami Barends, David DiVincenzo and Xuexin Xu for fruitful discussions and insightful comments. We acknowledge support from the Federal Ministry of Education and Research (BMBF) within the framework program “Quantum technologies – from basic research to market”, under the QSolid Project, Grant No. 13N16149.

## Appendix A: Bogoliubov Approach

The Bogoliubov Transformation approach is not so accurate when anharmonicity is non-negligible. Nevertheless, it provides a clear physical picture and intuition. It can be used as a guidance for developing more accurate methods.

Here we use one Bogoliubov transformation to diagonalize the harmonic part of the Hamiltonian. We also assume anharmonicities of the qubits remain unchanged.

The transformation is defined by a unitary transformation  $u_{mj}$ :

$$a_m = \sum_j u_{mj} \alpha_j$$

After the transformation the undriven Hamiltonian is diagonalized:

$$\begin{aligned} \tilde{H} &= U^\dagger H U \\ &= \sum_m \tilde{\omega}_m \alpha_m^\dagger \alpha_m + \frac{\delta_m}{2} \alpha_m^\dagger \alpha_m (\alpha_m^\dagger \alpha_m - 1) \end{aligned} \quad (\text{A1})$$

$$\tilde{H}_d = \sum_{mjk} \Omega_m u_{mj}^* u_{mk} \sin(\nu_m t + \phi_m^d) \alpha_j^\dagger \alpha_k$$

$$\begin{aligned} \tilde{H} &= \sum_m (\tilde{\omega}_m + \sum_j |u_{jm}|^2 \Omega_j \sin(\omega_j^d t + \phi_j)) \alpha_m^\dagger \alpha_m \\ &+ \frac{\delta_m}{2} \alpha_m^\dagger \alpha_m (\alpha_m^\dagger \alpha_m - 1) \\ &+ \sum_{mjk} \Omega_m \sin(\nu_m t + \phi_m^d) u_{mj}^* u_{mk} \alpha_j^\dagger \alpha_k \end{aligned}$$

Going to the rotating frame defined by  $U_r = e^{-i \int \sum_m (\tilde{\omega}_m + \sum_j |u_{jm}|^2 \Omega_j \sin(\omega_j^d t + \phi_j)) \alpha_m^\dagger \alpha_m dt}$ .

The resulting Hamiltonian takes the following form:

$$\begin{aligned} \tilde{H}_R &= \sum_{jk} \tilde{g}_{jk}(t) \alpha_j^\dagger \alpha_k \\ &+ \sum_m \frac{\delta_m}{2} \alpha_m^\dagger \alpha_m (\alpha_m^\dagger \alpha_m - 1) \end{aligned} \quad (\text{A2})$$

where

$$\begin{aligned} \tilde{g}_{jk} &= \sum_{n_0, n_1, n_2 = -\infty}^{+\infty} \sum_{m=0}^2 A_{n_0 n_1 n_2}^{jk}(m) \Omega_m u_{mj}^* u_{mk} i^{n_0 + n_1 + n_2} e^{i\phi(t)} \\ \phi(t) &= (\tilde{\omega}_j - \tilde{\omega}_k - n_0 \nu_0 - n_1 \nu_1 - n_2 \nu_2) t - n_0 \varphi_0 - n_1 \varphi_1 - n_2 \varphi_2 \end{aligned} \quad (\text{A3})$$

$$\begin{aligned} A_{n_0 n_1 n_2}^{jk}(0) &= \frac{J_{n_0+1}(-s_0^{jk}) + J_{n_0-1}(-s_0^{jk})}{2} J_{n_1}(-s_1^{jk}) J_{n_2}(-s_2^{jk}) \\ A_{n_0 n_1 n_2}^{jk}(1) &= J_{n_0}(-s_0^{jk}) \frac{J_{n_1+1}(-s_1^{jk}) + J_{n_1-1}(-s_1^{jk})}{2} J_{n_2}(-s_2^{jk}) \\ A_{n_0 n_1 n_2}^{jk}(2) &= J_{n_0}(-s_0^{jk}) J_{n_1}(-s_1^{jk}) \frac{J_{n_2+1}(-s_2^{jk}) + J_{n_2-1}(-s_2^{jk})}{2} \end{aligned} \quad (\text{A4})$$

$$s_m^{jk} = \frac{|u_{mj}|^2 - |u_{mk}|^2}{\nu_m} \Omega_m$$

$J_n$  is the  $n$ th Bessel function of the first kind.

## Appendix B: Analytical coupling strength by exact diagonalization

For more accuracy, one can numerically find the exact transformation to diagonalize the undriven Hamiltonian.

Assuming we can find the exact transformation  $U^{exa}$  for the undriven Hamiltonian  $H$ :

$$U = \sum u_{Q'_1 Q'_2 R', Q_1 Q_2 R} |Q'_1 Q'_2 R'\rangle \langle Q_1 Q_2 R|$$

The undriven Hamiltonian is diagonalised by this transformation:

$$\tilde{H} = U^\dagger H U = \sum_{Q_1 Q_2 R} \tilde{\omega}_{Q_1 Q_2 R} |Q_1 Q_2 R\rangle \langle Q_1 Q_2 R|$$

The drive Hamiltonian can be transformed to the diagonal frame by the same transformation  $U$ :

$$\begin{aligned} \tilde{H}_d &= U^\dagger H_d U \\ &= \sum_i \Omega_i \sin(\omega_i^d t + \phi_i) U^\dagger a_i^\dagger a_i U \end{aligned} \quad (\text{B1})$$

$U^\dagger a_i^\dagger a_i U$  can be numerically evaluated as well:

$$\begin{aligned} U^\dagger a_m^\dagger a_m U &= \sum |Q'_1 Q'_2 R'\rangle \langle Q'_1 Q'_2 R'| U^\dagger a_m^\dagger a_m U |Q_1 Q_2 R\rangle \langle Q_1 Q_2 R| \\ &= \sum \langle Q'_1 Q'_2 R'| U^\dagger a_m^\dagger a_m U |Q_1 Q_2 R\rangle |Q'_1 Q'_2 R'\rangle \langle Q_1 Q_2 R| \end{aligned} \quad (\text{B2})$$

Using the notations introduced in Eq.(17), we can split Eq.(B2) further into diagonal terms, which correspond to correction to energies, and off-diagonal terms, which couples different eigenstates of the undriven Hamiltonian:

$$\begin{aligned} U^\dagger a_m^\dagger a_m U &= \sum_{Q_1 Q_2 R} N_{Q_1 Q_2 R}^m |Q_1 Q_2 R\rangle \langle Q_1 Q_2 R| \\ &+ \sum_{Q'_1 Q'_2 R' \neq Q_1 Q_2 R} C_{Q'_1 Q'_2 R', Q_1 Q_2 R}^m |Q'_1 Q'_2 R'\rangle \langle Q_1 Q_2 R| \end{aligned} \quad (\text{B3})$$

Substituting Eq.(B3) into Eq.(B1) we get:

$$\begin{aligned}
\tilde{H}_d &= U^\dagger H_d U \\
&= \sum \Omega_m \sin(\nu_m t + \phi_m^d) (N_{Q_1 Q_2 R}^m |Q_1 Q_2 R\rangle \langle Q_1 Q_2 R| + C_{Q'_1 Q'_2 R', Q_1 Q_2 R}^m |Q'_1 Q'_2 R'\rangle \langle Q_1 Q_2 R|) \\
&= \sum \Omega_m \sin(\nu_m t + \phi_m^d) N_{Q_1 Q_2 R}^m |Q_1 Q_2 R\rangle \langle Q_1 Q_2 R| + \sum \Omega_m \sin(\nu_m t + \phi_m^d) C_{Q'_1 Q'_2 R', Q_1 Q_2 R}^m |Q'_1 Q'_2 R'\rangle \langle Q_1 Q_2 R|
\end{aligned} \tag{B4}$$

---

The total Hamiltonian now reads as follows:

---

$$\begin{aligned}
\tilde{H} &= \sum_{Q_1 Q_2 R} (\tilde{\omega}_{Q_1 Q_2 R} + \sum_m \Omega_m \sin(\nu_m t + \phi_m^d) N_{Q_1 Q_2 R}^m) |Q_1 Q_2 R\rangle \langle Q_1 Q_2 R| \\
&+ \sum_{m Q_1 Q_2 R \neq Q'_1 Q'_2 R'} \Omega_m \sin(\nu_m t + \phi_m^d) C_{Q'_1 Q'_2 R', Q_1 Q_2 R}^m |Q'_1 Q'_2 R'\rangle \langle Q_1 Q_2 R|
\end{aligned} \tag{B5}$$

---

The rotating frame is now defined by the transformation:

---

$$\begin{aligned}
U_r &= e^{-i \int \sum_{Q_1 Q_2 R} (\tilde{\omega}_{Q_1 Q_2 R} + \sum_m \Omega_m \sin(\nu_m t + \phi_m^d) N_{Q_1 Q_2 R}^m) |Q_1 Q_2 R\rangle \langle Q_1 Q_2 R| dt} \\
&= \sum_{Q_1 Q_2 R} e^{-i \int (\tilde{\omega}_{Q_1 Q_2 R} + \sum_m \Omega_m \sin(\nu_m t + \phi_m^d) N_{Q_1 Q_2 R}^m) dt} |Q_1 Q_2 R\rangle \langle Q_1 Q_2 R|
\end{aligned} \tag{B6}$$

The final Hamiltonian in the rotating frame can be calculated similarly as in the Bogoliubov case.

$$\tilde{H}_R = \sum G(t)_{Q'_1 Q'_2 R', Q_1 Q_2 R} |Q'_1 Q'_2 R'\rangle \langle Q_1 Q_2 R| \tag{B7}$$

where

$$\begin{aligned}
G(t)_{Q'_1 Q'_2 R', Q_1 Q_2 R} &= \sum_{n_0, n_1, n_2 = -\infty}^{+\infty} \sum_{m=0}^2 A_{n_0 n_1 n_2}^{Q'_1 Q'_2 R', Q_1 Q_2 R}(m) \Omega_m C_{Q'_1 Q'_2 R', Q_1 Q_2 R}^m i^{n_0 + n_1 + n_2} \\
&* e^{i((\tilde{\omega}_{Q'_1 Q'_2 R'} - \tilde{\omega}_{Q_1 Q_2 R} - n_0 \nu_0 - n_1 \nu_1 - n_2 \nu_2)t - n_0 \varphi_0 - n_1 \varphi_1 - n_2 \varphi_2)}
\end{aligned} \tag{B8}$$

$$\begin{aligned}
A_{n_0 n_1 n_2}^{Q'_1 Q'_2 R', Q_1 Q_2 R}(0) &= \frac{J_{n_0+1}(-s_0^{Q'_1 Q'_2 R', Q_1 Q_2 R}) + J_{n_0-1}(-s_0^{Q'_1 Q'_2 R', Q_1 Q_2 R})}{2} \\
&* J_{n_1}(-s_1^{Q'_1 Q'_2 R', Q_1 Q_2 R}) J_{n_2}(-s_2^{(ijk, npq)}) \\
A_{n_0 n_1 n_2}^{Q'_1 Q'_2 R', Q_1 Q_2 R}(1) &= J_{n_0}(-s_0^{Q'_1 Q'_2 R', Q_1 Q_2 R}) \\
&* \frac{J_{n_1+1}(-s_1^{Q'_1 Q'_2 R', Q_1 Q_2 R}) + J_{n_1-1}(-s_1^{Q'_1 Q'_2 R', Q_1 Q_2 R})}{2} \\
&* J_{n_2}(-s_2^{Q'_1 Q'_2 R', Q_1 Q_2 R}) \\
A_{n_0 n_1 n_2}^{Q'_1 Q'_2 R', Q_1 Q_2 R}(2) &= J_{n_0}(-s_0^{Q'_1 Q'_2 R', Q_1 Q_2 R}) J_{n_1}(-s_1^{Q'_1 Q'_2 R', Q_1 Q_2 R}) \\
&* \frac{J_{n_2+1}(-s_2^{Q'_1 Q'_2 R', Q_1 Q_2 R}) + J_{n_2-1}(-s_2^{Q'_1 Q'_2 R', Q_1 Q_2 R})}{2}
\end{aligned} \tag{B9}$$

---

Note that here the definition of coupling strength  $G(t)$

$$s_m^{Q'_1 Q'_2 R', Q_1 Q_2 R} = \frac{N_{Q'_1 Q'_2 R'}^m - N_{Q_1 Q_2 R}^m}{\nu_m} \Omega_m$$

is different from  $\tilde{g}(t)$  defined in Eq.(A2) by the factor  $\sqrt{(n_j + 1)n_k}$ . This factor is absorbed into the creation and annihilation operators in the Bogoliubov Transformation case.

The resonance condition is now given by:

$$\tilde{\omega}_{Q'_1 Q'_2 R'} - \tilde{\omega}_{Q_1 Q_2 R} - n_0 \nu_0 - n_1 \nu_1 - n_2 \nu_2 = 0 \quad (\text{B10})$$

### Appendix C: Details of crosstalk

Plots of crosstalk effects in Fig.(12).

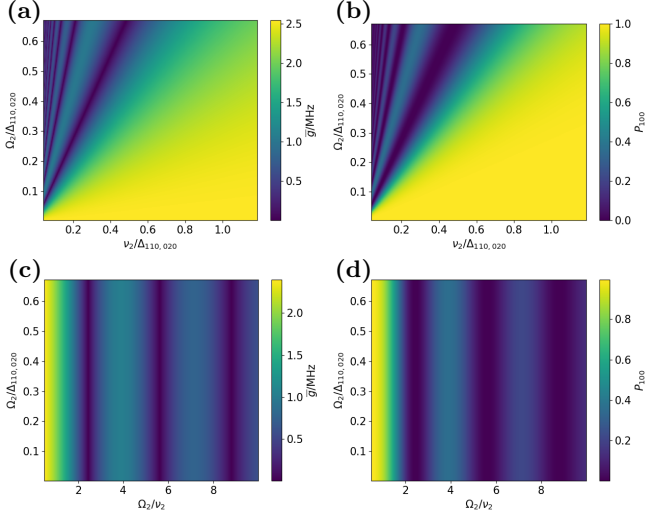


FIG. 12: Crosstalk effect of the second drive on the first drive. 12(a) Analytical calculation of static  $\bar{g}_{010,100}$  vs  $\Omega_2$  and  $\nu_2$  while the first drive is fixed at  $\Omega_1 = 150$  MHz,  $\nu_1 = \Delta_{010,100}$ . The analytical plot confirms the numerical simulation in Fig.(5). 12(b) Analytical calculation of P10 using the static coupling strength  $\bar{g}_{010,100}$ . 12(c) Analytical calculation of static  $\bar{g}_{010,100}$  vs  $\Omega_2$  and  $\frac{\Omega_2}{\nu_2}$  while the first drive is fixed at  $\Omega_1 = 150$  MHz,  $\nu_1 = \Delta_{010,100}$ . Zeros of  $J_0$  show up at  $\frac{\Omega_2}{\nu_2} = 2.40, 5.52, 8.65\dots$  12(d) Analytical calculation of P10 according to  $\bar{g}_{010,100}$  vs  $\Omega_2$  and  $\frac{\Omega_2}{\nu_2}$ .

### Appendix D: Minimizing Leakage

Plots of 2D scan of optimal drive amplitude in FFig.(13)

### Appendix E: Pulse Shaping

FIG.14 shows iswap and cphase parameters with pulse shaping.

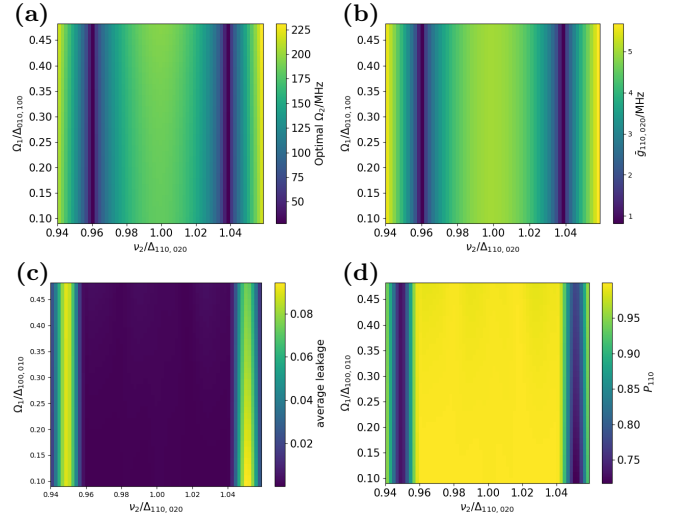


FIG. 13: Optimal  $\Omega_2$  and  $g_{110,020}$  vs  $\Omega_1$  and  $\nu_2$  and the corresponding leakage and  $P_{110}$ . 13(a) Analytically calculated optimal  $\Omega_2$  vs  $\nu_2$  and  $\Omega_1$ . The solvable area ( $|\nu_2 - \Delta_{110,020}| < \frac{2\pi}{t_g}$ ) is bounded by the two dark vertical lines indicating  $|\nu_2 - \Delta_{110,020}| = \frac{2\pi}{t_g}$ . 13(b) Analytically calculated optimal effective coupling  $\bar{g}_{110,020}$  vs  $\nu_2$  and  $\Omega_1$ . 13(c) Leakage vs  $\Omega_1$  and  $\nu_2$  from numerical simulation. The amplitude of the second drive  $\Omega_2$  is determined using the analytical formula. Within the solvable area, the leakage is consistently lower than 1%. 13(d)  $P_{110}$  vs  $\Omega_1$  and  $\nu_2$  from numerical simulation.



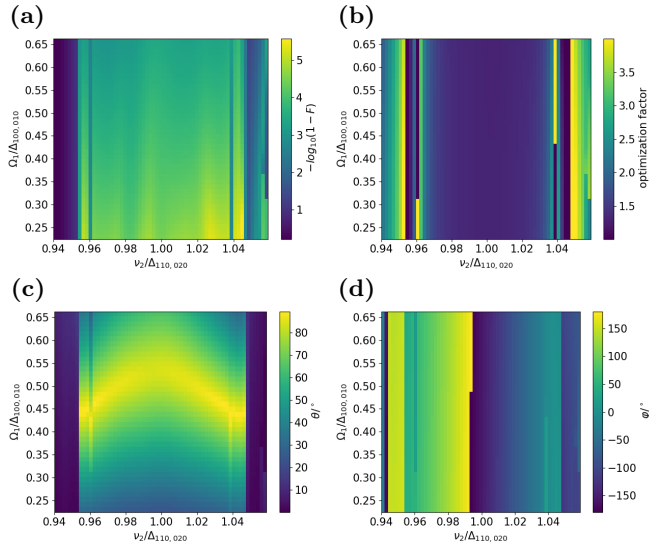


FIG. 14: fSim gate with flat-top Gaussian pulse-shaping. 14(a) Fidelity with pulse-shaping. The overall fidelity is improved by almost one order of magnitude. 14(b) Optimization factor for pulse-shaping. The discontinuity in the optimization factor is the reason for the jumps/discontinuity in fidelity,  $\theta$  and  $\varphi$ . 14(c) Numerically calculated  $P_{100}$  vs  $\Omega_1$  and  $\nu_2$  14(d) Numerically calculated conditional phase vs  $\Omega_1$  and  $\nu_2$ . The plot is more irregular due to the optimization needed for pulse-shaping.

- [1] D. Gottesman, [Stabilizer codes and quantum error correction](#) (1997), [arXiv:quant-ph/9705052 \[quant-ph\]](#).
- [2] F. Arute, K. Arya, R. Babbush, D. Bacon, J. C. Bardin, R. Barends, R. Biswas, S. Boixo, F. G. Brandao, D. A. Buell, *et al.*, Quantum supremacy using a programmable superconducting processor, *Nature* **574**, 505 (2019).
- [3] R. Acharya, I. Aleiner, R. Allen, T. I. Andersen, M. Ansmann, F. Arute, K. Arya, A. Asfaw, J. Atalaya, R. Babbush, D. Bacon, J. C. Bardin, J. Basso, A. Bengtsson, S. Boixo, G. Bortoli, A. Bourassa, J. Bovaird, L. Brill, M. Broughton, B. B. Buckley, D. A. Buell, T. Burger, B. Burkett, N. Bushnell, Y. Chen, Z. Chen, B. Chiaro, J. Cogan, R. Collins, P. Conner, W. Courtney, A. L. Crook, B. Curtin, D. M. Debroy, A. Del Toro Barba, S. Demura, A. Dunsworth, D. Eppens, C. Erickson, L. Faoro, E. Farhi, R. Fatemi, L. Flores Burgos, E. Forati, A. G. Fowler, B. Foxen, W. Giang, C. Gidney, D. Gilboa, M. Giustina, A. Grajales Dau, J. A. Gross, S. Habegger, M. C. Hamilton, M. P. Harrigan, S. D. Harrington, O. Higgott, J. Hilton, M. Hoffmann, S. Hong, T. Huang, A. Huff, W. J. Huggins, L. B. Ioffe, S. V. Isakov, J. Iveland, E. Jeffrey, Z. Jiang, C. Jones, P. Juhas, D. Kafri, K. Kechedzhi, J. Kelly, T. Khatarr, M. Khezri, M. Kieferová, S. Kim, A. Kitaev, P. V. Klimov, A. R. Klots, A. N. Korotkov, F. Kostritsa, J. M. Kreikebaum, D. Landhuis, P. Laptev, K.-M. Lau, L. Laws, J. Lee, K. Lee, B. J. Lester, A. Lill, W. Liu, A. Locharla, E. Lucero, F. D. Malone, J. Marshall, O. Martin, J. R. McClean, T. McCourt, M. McEwen, A. Megrant, B. Meurer Costa, X. Mi, K. C. Miao, M. Mohseni, S. Montazeri, A. Morvan, E. Mount, W. Mruczkiewicz, O. Naaman, M. Neeley, C. Neill, A. Nersisyan, H. Neven, M. Newman, J. H. Ng, A. Nguyen, M. Nguyen, M. Y. Niu, T. E. O'Brien, A. Opremcak, J. Platt, A. Petukhov, R. Potter, L. P. Pryadko, C. Quintana, P. Roushan, N. C. Rubin, N. Saei, D. Sank, K. Sankaragomathi, K. J. Satzinger, H. F. Schurkus, C. Schuster, M. J. Shearn, A. Shorter, V. Shvarts, J. Skrzuzny, V. Smelyanskiy, W. C. Smith, G. Sterling, D. Strain, M. Szalay, A. Torres, G. Vidal, B. Villalonga, C. Vollgraf Heidweiller, T. White, C. Xing, Z. J. Yao, P. Yeh, J. Yoo, G. Young, A. Zalcman, Y. Zhang, N. Zhu, and G. Q. AI, Suppressing quantum errors by scaling a surface code logical qubit, *Nature* **614**, 676 (2023).
- [4] M. Mohseni, A. Scherer, K. G. Johnson, O. Wertheim, M. Otten, N. A. Aadit, K. M. Bresniker, K. Y. Camasari, B. Chapman, S. Chatterjee, G. A. Dagnew, A. Esposito, F. Fahim, M. Fiorentino, A. Khalid, X. Kong, B. Kulchytskyy, R. Li, P. A. Lott, I. L. Markov, R. F. McDermott, G. Pedretti, A. Gajjar, A. Silva, J. Sorebo, P. Spentzouris, Z. Steiner, B. Torosov, D. Venturelli, R. J. Visser, Z. Webb, X. Zhan, Y. Cohen, P. Ronagh, A. Ho, R. G. Beausoleil, and J. M. Martinis, [How to build a quantum supercomputer: Scaling challenges and opportunities](#) (2024), [arXiv:2411.10406 \[quant-ph\]](#).
- [5] S. Bravyi, O. Dial, J. M. Gambetta, D. Gil, and Z. Nazario, The future of quantum computing with superconducting qubits, *Journal of Applied Physics* **132**, 10.1063/5.0082975 (2022).
- [6] H. Xiong, Q. Ficheux, A. Somoroff, L. B. Nguyen, E. Dogan, D. Rosenstock, C. Wang, K. N. Nesterov, M. G. Vavilov, and V. E. Manucharyan, Arbitrary controlled-phase gate on fluxonium qubits using differential ac stark shifts, *Phys. Rev. Res.* **4**, 023040 (2022).
- [7] E. A. Sete, N. Didier, A. Q. Chen, S. Kulshreshtha, R. Manenti, and S. Poletto, Parametric-resonance entangling gates with a tunable coupler, *Phys. Rev. Appl.* **16**, 024050 (2021).
- [8] P. K. Barkoutsos, J. F. Gonthier, I. Sokolov, N. Moll, G. Salis, A. Fuhrer, M. Ganzhorn, D. J. Egger, M. Troyer, A. Mezzacapo, S. Filipp, and I. Tavernelli, Quantum algorithms for electronic structure calculations: Particle-hole hamiltonian and optimized wave-function expansions, *Phys. Rev. A* **98**, 022322 (2018).
- [9] F. Motzoi, M. P. Kaicher, and F. K. Wilhelm, Linear and logarithmic time compositions of quantum many-body operators, *Phys. Rev. Lett.* **119**, 160503 (2017).
- [10] M. McEwen, K. C. Miao, J. Atalaya, A. Bilmes, A. Crook, J. Bovaird, J. M. Kreikebaum, N. Zobrist, E. Jeffrey, B. Ying, A. Bengtsson, H.-S. Chang, A. Dunsworth, J. Kelly, Y. Zhang, E. Forati, R. Acharya, J. Iveland, W. Liu, S. Kim, B. Burkett, A. Megrant, Y. Chen, C. Neill, D. Sank, M. Devoret, and A. Opremcak, [Resisting high-energy impact events through gap engineering in superconducting qubit arrays](#) (2024), [arXiv:2402.15644 \[quant-ph\]](#).
- [11] R. Benevides, M. Drimmer, G. Bisson, F. Adinolfi, U. Lüpke, H. Döeleman, G. Catelani, and Y. Chu, Quasiparticle dynamics in a superconducting qubit irradiated by a localized infrared source, *Physical Review Letters* **133**, 10.1103/physrevlett.133.060602 (2024).
- [12] M. Bal, M. H. Ansari, J.-L. Orgiazzi, R. M. Lutchyn, and A. Lupascu, Dynamics of parametric fluctuations induced by quasiparticle tunneling in superconducting flux qubits, *Phys. Rev. B* **91**, 195434 (2015).
- [13] M. H. Ansari, Rate of tunneling nonequilibrium quasiparticles in superconducting qubits, *Superconductor Science and Technology* **28**, 045005 (2015).
- [14] J. Lisenfeld, A. Bilmes, and A. V. Ustinov, Enhancing the coherence of superconducting quantum bits with electric fields, *npj Quantum Information* **9**, 8 (2023).
- [15] M. H. Ansari, F. K. Wilhelm, U. Sinha, and A. Sinha, The effect of environmental coupling on tunneling of quasiparticles in josephson junctions, *Superconductor Science and Technology* **26**, 125013 (2013).
- [16] X. Xu, Manabputra, C. Vignes, M. H. Ansari, and J. M. Martinis, [Lattice hamiltonians and stray interactions within quantum processors](#), <https://arxiv.org/abs/2402.09145> (2024), [arXiv:2402.09145 \[quant-ph\]](#).
- [17] X. Xu and M. Ansari, *zz* freedom in two-qubit gates, *Phys. Rev. Appl.* **15**, 064074 (2021).
- [18] X. Xu and M. Ansari, Parasitic-free gate: An error-protected cross-resonance switch in weakly tunable architectures, *Phys. Rev. Appl.* **19**, 024057 (2023).
- [19] J. Preskill, Quantum Computing in the NISQ era and beyond, *Quantum* **2**, 79 (2018).
- [20] L. Egan, D. M. Debroy, C. Noel, A. Risinger, D. Zhu, D. Biswas, M. Newman, M. Li, K. R. Brown, M. Cetina, and C. Monroe, Fault-tolerant control of an error-corrected qubit, *Nature* **598**, 281 (2021).

- [21] J. Pazem and M. H. Ansari, Error mitigation of entangled states using brainbox quantum autoencoders, arXiv preprint arXiv:2303.01134 (2023).
- [22] I. M. Georgescu, S. Ashhab, and F. Nori, Quantum simulation, *Rev. Mod. Phys.* **86**, 153 (2014).
- [23] A. J. Daley, I. Bloch, C. Kokail, S. Flannigan, N. Pearson, M. Troyer, and P. Zoller, Practical quantum advantage in quantum simulation, *Nature* **607**, 667 (2022).
- [24] C. W. Bauer, Z. Davoudi, A. B. Balantekin, T. Bhattacharya, M. Carena, W. A. de Jong, P. Draper, A. El-Khadra, N. Gemelke, M. Hanada, D. Kharzeev, H. Lamm, Y.-Y. Li, J. Liu, M. Lukin, Y. Meurice, C. Monroe, B. Nachman, G. Pagano, J. Preskill, E. Rinaldi, A. Roggero, D. I. Santiago, M. J. Savage, I. Siddiqi, G. Siopsis, D. V. Zanten, N. Wiebe, Y. Yamauchi, K. Yeter-Aydeniz, and S. Zorzetti, Quantum simulation for high energy physics (2022), arXiv:2204.03381 [quant-ph].
- [25] Evidence for the utility of quantum computing before fault tolerance, *Nature* **618**, 500 (2023).
- [26] F. Verstraete, J. I. Cirac, and J. I. Latorre, Quantum circuits for strongly correlated quantum systems, *Phys. Rev. A* **79**, 032316 (2009).
- [27] I. D. Kivlichan, J. McClean, N. Wiebe, C. Gidney, A. Aspuru-Guzik, G. K.-L. Chan, and R. Babbush, Quantum simulation of electronic structure with linear depth and connectivity, *Phys. Rev. Lett.* **120**, 110501 (2018).
- [28] C. Cade, L. Mineh, A. Montanaro, and S. Stanisic, Strategies for solving the fermi-hubbard model on near-term quantum computers, *Phys. Rev. B* **102**, 235122 (2020).
- [29] B. Foxen, C. Neill, A. Dunsworth, P. Roushan, B. Chiaro, A. Megrant, J. Kelly, Z. Chen, K. Satzinger, R. Barends, F. Arute, K. Arya, R. Babbush, D. Bacon, J. C. Bardin, S. Boixo, D. Buell, B. Burkett, Y. Chen, R. Collins, E. Farhi, A. Fowler, C. Gidney, M. Giustina, R. Graff, M. Harrigan, T. Huang, S. V. Isakov, E. Jeffrey, Z. Jiang, D. Kafri, K. Kechedzhi, P. Klimov, A. Korotkov, F. Kostritsa, D. Landhuis, E. Lucero, J. McClean, M. McEwen, X. Mi, M. Mohseni, J. Y. Mutus, O. Naaman, M. Neeley, M. Niu, A. Petukhov, C. Quintana, N. Rubin, D. Sank, V. Smelyanskiy, A. Vainsencher, T. C. White, Z. Yao, P. Yeh, A. Zalcman, H. Neven, and J. M. Martinis (Google AI Quantum), Demonstrating a continuous set of two-qubit gates for near-term quantum algorithms, *Phys. Rev. Lett.* **125**, 120504 (2020).
- [30] I. N. Moskalkenko, I. A. Simakov, N. N. Abramov, A. A. Grigorev, D. O. Moskalev, A. A. Pishchimova, N. S. Smirnov, E. V. Zikiy, I. A. Rodionov, and I. S. Besedin, High fidelity two-qubit gates on fluxoniums using a tunable coupler, *npj Quantum Information* **8**, 130 (2022).
- [31] N. Lacroix, C. Hellings, C. K. Andersen, A. Di Paolo, A. Remm, S. Lazar, S. Krinner, G. J. Norris, M. Gabureac, J. Heinsoo, A. Blais, C. Eichler, and A. Wallraff, Improving the performance of deep quantum optimization algorithms with continuous gate sets, *PRX Quantum* **1**, 020304 (2020).
- [32] M. Ganzhorn, D. Egger, P. Barkoutsos, P. Ollitrault, G. Salis, N. Moll, M. Roth, A. Fuhrer, P. Mueller, S. Wöerner, I. Tavernelli, and S. Filipp, Gate-efficient simulation of molecular eigenstates on a quantum computer, *Phys. Rev. Appl.* **11**, 044092 (2019).
- [33] M. G. Algaba, P. V. Sriluckshmy, M. Leib, and F. Šimkovic IV, Low-depth simulations of fermionic systems on square-grid quantum hardware, *Quantum* **8**, 1327 (2024).
- [34] F. Verstraete, J. I. Cirac, and J. I. Latorre, Quantum circuits for strongly correlated quantum systems, *Phys. Rev. A* **79**, 032316 (2009).
- [35] M. A. Nielsen, The fermionic canonical commutation relations and the jordan-wigner transform (2005).
- [36] M. Reagor, C. B. Osborn, N. Tezak, A. Staley, G. Prawiroatmodjo, M. Scheer, N. Alidoust, E. A. Sete, N. Didier, M. P. da Silva, E. Acala, J. Angeles, A. Bestwick, M. Block, B. Bloom, A. Bradley, C. Bui, S. Caldwell, L. Capelluto, R. Chilcott, J. Cordova, G. Crossman, M. Curtis, S. Deshpande, T. El Bouayadi, D. Girshovich, S. Hong, A. Hudson, P. Karalekas, K. Kuang, M. Lenihan, R. Manenti, T. Manning, J. Marshall, Y. Mohan, W. O'Brien, J. Otterbach, A. Papageorge, J.-P. Paquette, M. Pelstring, A. Polloreno, V. Rawat, C. A. Ryan, R. Renzas, N. Rubin, D. Russel, M. Rust, D. Scarabelli, M. Selvanayagam, R. Sinclair, R. Smith, M. Suska, T.-W. To, M. Vahidpour, N. Vodrahalli, T. Whyland, K. Yadav, W. Zeng, and C. T. Rigetti, Demonstration of universal parametric entangling gates on a multi-qubit lattice, *Science Advances* **4**, 10.1126/sciadv.aao3603 (2018).
- [37] S. Caldwell, N. Didier, C. Ryan, E. Sete, A. Hudson, P. Karalekas, R. Manenti, M. da Silva, R. Sinclair, E. Acala, *et al.*, Parametrically activated entangling gates using transmon qubits, *Physical Review Applied* **10**, 034050 (2018).
- [38] T. McBroom-Carroll, A. Schlabes, X. Xu, J. Ku, B. Cole, S. Indrajeet, M. D. LaHaye, M. H. Ansari, and B. L. T. Plourde, Entangling interactions between artificial atoms mediated by a multimode left-handed superconducting ring resonator, *PRX Quantum* **5**, 020325 (2024).
- [39] C. Scarato, C. Hellings, K. Hanke, A. Remm, S. Lazar, D. Colao Zanuz, M. Kerschbaum, N. Lacroix, J. Herrmann, F. Swiadek, G. Norris, M. Bahrami Panah, A. Flasby, C. Eichler, and A. Wallraff, Robust hardware-efficient implementation of a continuous two-qubit gate set for transmon qubits, in *APS March Meeting Abstracts*, APS Meeting Abstracts, Vol. 2023 (2023) p. Y64.005.
- [40] S. Li, J. Xue, T. Chen, and Z.-Y. Xue, High-fidelity geometric quantum gates with short paths on superconducting circuits, *Advanced Quantum Technologies* **4**, 2000140 (2021).
- [41] J. Koch, T. M. Yu, J. Gambetta, A. A. Houck, D. I. Schuster, J. Majer, A. Blais, M. H. Devoret, S. M. Girvin, and R. J. Schoelkopf, Charge-insensitive qubit design derived from the cooper pair box, *Phys. Rev. A* **76**, 042319 (2007).
- [42] P. Bertet, C. J. P. M. Harmans, and J. E. Mooij, Parametric coupling for superconducting qubits, *Phys. Rev. B* **73**, 064512 (2006).
- [43] A. Niskanen, K. Harrabi, F. Yoshihara, Y. Nakamura, S. Lloyd, and J. S. Tsai, Quantum coherent tunable coupling of superconducting qubits, *Science* **316**, 723 (2007).
- [44] A. O. Niskanen, Y. Nakamura, and J.-S. Tsai, Tunable coupling scheme for flux qubits at the optimal point, *Phys. Rev. B* **73**, 094506 (2006).
- [45] F. Beaudoin, M. P. da Silva, Z. Dutton, and A. Blais, First-order sidebands in circuit qed using qubit frequency modulation, *Phys. Rev. A* **86**, 022305 (2012).

- [46] J. D. Strand, M. Ware, F. Beaudoin, T. A. Ohki, B. R. Johnson, A. Blais, and B. L. T. Plourde, First-order sideband transitions with flux-driven asymmetric transmon qubits, *Phys. Rev. B* **87**, 220505 (2013).
- [47] B. Royer, A. L. Grimsmo, N. Didier, and A. Blais, Fast and high-fidelity entangling gate through parametrically modulated longitudinal coupling, *Quantum* **1**, 11 (2017).
- [48] R. Naik, N. Leung, S. Chakram, P. Groszkowski, Y. Lu, N. Earnest, D. McKay, J. Koch, and D. I. Schuster, Random access quantum information processors using multimode circuit quantum electrodynamics, *Nature communications* **8**, 1904 (2017).
- [49] D. C. McKay, S. Filipp, A. Mezzacapo, E. Magesan, J. M. Chow, and J. M. Gambetta, Universal gate for fixed-frequency qubits via a tunable bus, *Phys. Rev. Appl.* **6**, 064007 (2016).
- [50] M. Ganzhorn, G. Salis, D. J. Egger, A. Fuhrer, M. Mergenthaler, C. Müller, P. Müller, S. Paredes, M. Pechal, M. Werninghaus, and S. Filipp, Benchmarking the noise sensitivity of different parametric two-qubit gates in a single superconducting quantum computing platform, *Phys. Rev. Res.* **2**, 033447 (2020).
- [51] A. Blais, A. L. Grimsmo, S. M. Girvin, and A. Wallraff, Circuit quantum electrodynamics, *Rev. Mod. Phys.* **93**, 025005 (2021).
- [52] M. F. Gely, G. A. Steele, and D. Bothner, Nature of the lamb shift in weakly anharmonic atoms: From normal-mode splitting to quantum fluctuations, *Phys. Rev. A* **98**, 053808 (2018).
- [53] M. H. Ansari, Superconducting qubits beyond the dispersive regime, *Phys. Rev. B* **100**, 024509 (2019).
- [54] M. Xia, C. Zhou, C. Liu, P. Patel, X. Cao, P. Lu, B. Mesits, M. Mucci, D. Gorski, D. Pekker, and M. Hatridge, Fast superconducting qubit control with subharmonic drives (2023), [arXiv:2306.10162 \[quant-ph\]](https://arxiv.org/abs/2306.10162).
- [55] J. Ku, X. Xu, M. Brink, D. C. McKay, J. B. Hertzberg, M. H. Ansari, and B. L. Plourde, Suppression of Unwanted ZZ Interactions in a Hybrid Two-Qubit System, *Physical review letters* **125**, 200504 (2020), [arXiv:2003.02775](https://arxiv.org/abs/2003.02775).
- [56] J. Strand, M. Ware, F. Beaudoin, T. Ohki, B. Johnson, A. Blais, and B. Plourde, First-order sideband transitions with flux-driven asymmetric transmon qubits, *Physical Review B—Condensed Matter and Materials Physics* **87**, 220505 (2013).
- [57] L. H. Pedersen, N. M. Møller, and K. Mølmer, Fidelity of quantum operations, *Physics Letters A* **367**, 47 (2007).
- [58] D. Bluvstein, S. J. Evered, A. A. Geim, S. H. Li, H. Zhou, T. Manovitz, S. Ebadi, M. Cain, M. Kalinowski, D. Hangleiter, J. P. B. Ataiades, N. Maskara, I. Cong, X. Gao, P. S. Rodriguez, T. Karolyshyn, G. Semeghini, M. J. Gullans, M. Greiner, V. Vuletić, and M. D. Lukin, Logical quantum processor based on reconfigurable atom arrays, *Nature* , 1 (2023).
- [59] B. Barak and K. Marwaha, Classical algorithms and quantum limitations for maximum cut on high-girth graphs (Schloss Dagstuhl - Leibniz-Zentrum für Informatik, 2022).
- [60] B. Cheng, X.-H. Deng, X. Gu, Y. He, G. Hu, P. Huang, J. Li, B.-C. Lin, D. Lu, Y. Lu, *et al.*, Noisy intermediate-scale quantum computers, *Frontiers of Physics* **18**, 21308 (2023).
- [61] M. H. Ansari, Entropy production in a photovoltaic cell, *Phys. Rev. B* **95**, 174302 (2017).
- [62] M. H. Ansari, A. van Steensel, and Y. V. Nazarov, Entropy production in quantum is different, *Entropy* **21**, 854 (2019).
- [63] M. H. Ansari and Y. V. Nazarov, Exact correspondence between Renyi entropy flows and physical flows, *Phys. Rev. B* **91**, 174307 (2015).
- [64] A. Schlabes, R. Bhowmick, and M. H. Ansari, *Fast gates of detuned cat qubit* (2024), [arXiv:2407.20820 \[quant-ph\]](https://arxiv.org/abs/2407.20820).
- [65] M. Ansari and Y. V. Nazarov, Keldysh formalism for multiple parallel worlds, *Journal of Experimental and Theoretical Physics* **122**, 389 (2016).
- [66] M. H. Ansari and Y. V. Nazarov, Rényi entropy flows from quantum heat engines, *Phys. Rev. B* **91**, 104303 (2015).
- [67] M. Ansari, M. Luján, C. Kotselidis, K. Jarvis, C. Kirkham, and I. Watson, Robust adaptation to available parallelism in transactional memory applications, in *Transactions on High-Performance Embedded Architectures and Compilers III*, edited by P. Stenstrom (Springer Berlin Heidelberg, Berlin, Heidelberg, 2011) pp. 236–255.
- [68] T. Roy, S. Kundu, M. Chand, S. Hazra, N. Nehra, R. Cosmic, A. Ranadive, M. P. Patankar, K. Damle, and R. Vijay, Implementation of pairwise longitudinal coupling in a three-qubit superconducting circuit, *Phys. Rev. Appl.* **7**, 054025 (2017).
- [69] K. Bharti, A. Cervera-Lierta, T. H. Kyaw, T. Haug, S. Alperin-Lea, A. Anand, M. Degroote, H. Heimonen, J. S. Kottmann, T. Menke, W.-K. Mok, S. Sim, L.-C. Kwek, and A. Aspuru-Guzik, Noisy intermediate-scale quantum algorithms, *Rev. Mod. Phys.* **94**, 015004 (2022).
- [70] E. Farhi, J. Goldstone, and S. Gutmann, A quantum approximate optimization algorithm (2014), [arXiv:1411.4028 \[quant-ph\]](https://arxiv.org/abs/1411.4028).
- [71] B. Pokharel and D. A. Lidar, Demonstration of algorithmic quantum speedup, *Phys. Rev. Lett.* **130**, 210602 (2023).
- [72] S. Basu, J. Born, A. Bose, S. Capponi, D. Chalkia, T. A. Chan, H. Doga, M. Goldsmith, T. Gujarati, A. Guzman-Saenz, D. Iliopoulos, G. O. Jones, S. Knecht, D. Madan, S. Maniscalco, N. Mariella, J. A. Morrone, K. Najafi, P. Pati, D. Platt, M. A. Rapsomaniki, A. Ray, K. Rhrissorakrai, O. Shehab, I. Tavernelli, M. Tolunay, F. Utro, S. Woerner, S. Zhuk, J. M. Garcia, and L. Parida, Towards quantum-enabled cell-centric therapeutics (2023), [arXiv:2307.05734 \[quant-ph\]](https://arxiv.org/abs/2307.05734).
- [73] C. Ryan-Anderson, J. G. Bohnet, K. Lee, D. Gresh, A. Hankin, J. P. Gaebler, D. Francois, A. Chernoguzov, D. Lucchetti, N. C. Brown, T. M. Gatterman, S. K. Halit, K. Gilmore, J. A. Gerber, B. Neyenhuis, D. Hayes, and R. P. Stutz, Realization of real-time fault-tolerant quantum error correction, *Phys. Rev. X* **11**, 041058 (2021).
- [74] M. H. Abobeih, Y. Wang, J. Randall, S. J. H. Loenen, C. E. Bradley, M. L. Markham, D. J. Twitchen, B. M. Terhal, and T. H. Taminiau, Fault-tolerant operation of a logical qubit in a diamond quantum processor, *Nature* **606**, 884 (2021).
- [75] S. Krinner, N. Lacroix, A. Remm, A. Di Paolo, E. Genois, C. Leroux, C. Hellings, S. Lazar, F. Swiadek, J. Herrmann, *et al.*, Realizing repeated quantum error correction in a distance-three surface code, *Nature* **605**, 669 (2022).

- [76] Y. Zhao, Y. Ye, H.-L. Huang, Y. Zhang, D. Wu, H. Guan, Q. Zhu, Z. Wei, T. He, S. Cao, F. Chen, T.-H. Chung, H. Deng, D. Fan, M. Gong, C. Guo, S. Guo, L. Han, N. Li, S. Li, Y. Li, F. Liang, J. Lin, H. Qian, H. Rong, H. Su, L. Sun, S. Wang, Y. Wu, Y. Xu, C. Ying, J. Yu, C. Zha, K. Zhang, Y.-H. Huo, C.-Y. Lu, C.-Z. Peng, X. Zhu, and J.-W. Pan, Realization of an error-correcting surface code with superconducting qubits, *Phys. Rev. Lett.* **129**, 030501 (2022).
- [77] N. Ofek, A. Petrenko, R. W. Heeres, P. Reinhold, Z. Leghtas, B. Vlastakis, Y. Liu, L. Frunzio, S. M. Girvin, L. Jiang, M. Mirrahimi, M. H. Devoret, and R. J. Schoelkopf, Extending the lifetime of a quantum bit with error correction in superconducting circuits, *Nature* **536**, 441 (2016).
- [78] A. Barenco, C. H. Bennett, R. Cleve, D. P. DiVincenzo, N. Margolus, P. Shor, T. Sleator, J. A. Smolin, and H. Weinfurter, Elementary gates for quantum computation, *Phys. Rev. A* **52**, 3457 (1995).
- [79] N. Khaneja and S. J. Glaser, Cartan decomposition of  $su(2^n)$ , constructive controllability of spin systems and universal quantum computing, *arXiv: Quantum Physics* (2000).
- [80] M. Ippoliti, K. Kechedzhi, R. Moessner, S. Sondhi, and V. Khemani, Many-body physics in the nisq era: Quantum programming a discrete time crystal, *PRX Quantum* **2**, 030346 (2021).